CRYSTAL GROWTH & DESIGN

pubs.acs.org/crystal

Article

Mechanistic Insights on Solution-Based Green Synthesis of Phase-Pure Ca-Based Layered Double Hydroxides from $Ca(OH)_2$

Maria C. Curria and Claire E. White*

Cite This: *Cryst. Growth Des.* 2024, 24, 56−70

Read Online

ACCESS | Metrics & More | Article Recommendations | Supporting Information

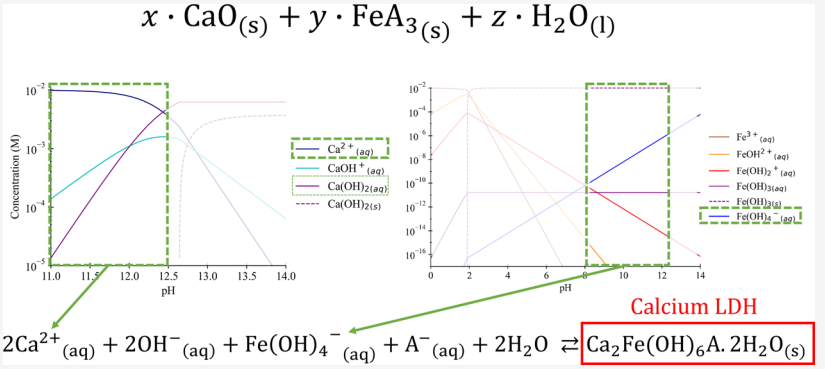

ABSTRACT: Ca-based layered double hydroxides (LDHs) are ideal candidates for applications that require the selective adsorption of anions and acidic molecules due to their positively charged layers and high density of exposed basic adsorption sites. As such, they are rapidly gaining attention in the fields of drug delivery, alloy corrosion inhibition, industrial waste recycling, environmental remediation, and CO_2 capture. Traditional LDH synthesis methods such as coprecipitation, urea hydrolysis, and sol−gel require use of non-environmentally friendly precursors and/or additional post-synthetic treatments to achieve highly crystalline and phase-pure Ca-LDHs. More recently, green synthesis of crystalline Ca-LDH has been achieved by means of $Ca(OH)_2$ hydrolysis without the need for strong alkalis (e.g., NaOH); however, attainment of phase-pure Ca-LDHs using this approach remains elusive due to a lack of understanding of the Ca-LDH formation mechanism. In this work, we develop a comprehensive solution speciation model for the synthesis of $Ca_2Fe(OH)_6Cl{\cdot}2H_2O$ via $Ca(OH)_2$ hydrolysis and discuss the effect of initial Ca/Fe(III) solution molar ratio ($SMR_{Ca/Fe}$) on sample purity and crystallinity from both a theoretical and experimental viewpoint. Our calculations show a $SMR_{Ca/Fe} \approx 3$ is needed to (i) achieve full conversion of the solid precursors and (ii) avoid the coprecipitation of less soluble impurities. This value stems from the chemical equilibria of species in solution and the need to be above a specific pH level to drive the precipitation of the Ca-LDH. Characterization of the samples using thermogravimetric analysis (TGA) coupled with gas Fourier transform infrared spectroscopy (gas-FTIR), high-resolution X-ray diffraction (HR-XRD), and pair distribution function analysis (PDF) supports the theoretical findings, showing evidence of high purity samples synthesized with $SMR_{Ca/Fe} \approx 3$. Based on these results, we introduce a new simplified method for the green synthesis of crystalline Ca-LDHs of different chemistries via in situ hydrolysis of $Ca(OH)_2$, consisting of a one-pot synthesis at ambient temperature without the need for strong alkalis (i.e., NaOH).

1. INTRODUCTION

The adsorptive and catalytic properties of layered double hydroxides (LDHs) in conjunction with their chemical versatility makes them ideal candidates for a broad range of applications, such as energy conversion and storage, heterogeneous catalysis, environmental remediation, and drug delivery, among others.[1−8] For example, LDHs with photo-active substitutes (such as Zn^{2+}), can be used as semiconductors in photo-catalytic applications, including water splitting for the production of H_2,[9−11] CO_2 conversion to methanol or CO,[12] and N_2 reduction into NH_3.[13] Ca-based LDHs, also known as hydrocalumite-like compounds (HClcs) due to their similarity to hydrocalumite ($Ca_2Al(OH)_6Cl{\cdot}2H_2O$), are mostly being studied for applications that involve anionic exchange or selective adsorption of acidic molecules.[14] Such is the case for some drug delivery systems, alloy corrosion inhibition, industrial waste recycling, environmental remediation, and CO_2 capture where higher purity of crystalline Ca-LDHs has been associated with increase in adsorption capacity.[15−22] Ca-LDHs are also relevant to the cement industry as they

Received: April 11, 2023
Revised: June 28, 2023
Accepted: June 29, 2023
Published: December 14, 2023

Table 1. Sample Identification, Concentrations of the Starting Precursor Solutions, Observations Made on Supernatant Solutions and Powder Samples, and Phase Identification and Purity of Final Powder Samples Synthesized Using the Modified Coprecipitation Method[a]

ID	SMR Ca/Fe	amount of precursors in ml (±0.1 mL)		supernatant solution		final powder sample		
		$Ca(OH)_2$ 0.2 M	$FeCl_3$ 0.1 M	color	pH (±0.5)	color	phases in XRD	purity from TGA ($\%m_{LDH}/m_{tot}$)
S10	10	50	10	clear	12.5	white	C, P, L	52.0
S5	5	50	20	clear	12.5	white	P, L	67.0
S3	3	50	33	clear	12.5	tan	L	91.0
S2	2	50	50	orange	11.0	orange	L, F	—[b]
S1	1	50	100	dark red	2.5	dark brown	F	—[b]

[a]C: calcite, P: portlandite, L: crystalline $Ca_2Fe(OH)_6Cl.\ 2H_2O_{(s)}$, F: amorphous 2-line ferrihydrite. [b]The model-fitting approach used to calculate purity from TGA was only applicable to samples containing both LDH and unreacted $Ca(OH)_2$.

constitute the AFm phases in hydrated Portland cement. Because AFm phases do not form solid solutions, but rather stay in a heterogeneous mix in cement paste, being able to synthesize phase-pure variants of Ca-LDHs allows for a better characterization of AFm phases in Portland cement.[23] However, the green synthesis of crystalline Ca-LDHs with high phase purity remains a challenge.

LDHs are anionic clays consisting of bimetallic hydroxide layers where the difference in the oxidation states of the metals within a layer creates a positive charge that is counteracted by hydrated interlayer anions.[24] The general composition of LDHs is usually expressed as $[M^{2+}_{1-x}M^{3+}_x(OH^-)_2]^{x+}[A^{n-}_{x/n}\cdot mH_2O]^{x-}$, where $[M^{2+}_{1-x}M^{3+}_x(OH^-)_2]^{x+}$ is the bimetallic hydroxide layer structure with divalent and trivalent metal cations M^{2+} and M^{3+}, and $[A^{n-}_{x/n}\cdot mH_2O]^{x-}$ describes the interlayer composition with A^{n-} being the interlayer anion of valence n and mH_2O being the interlayer water.[22,25−27] It has been shown that the chemical composition of an LDH directly impacts its properties,[28,29] where the composition can be controlled by means of an appropriate synthesis method and the careful selection of precursors.[29−35]

The most commonly reported synthesis route for LDHs is the coprecipitation method, which consists of mixing two solutions of divalent and trivalent metal salts with a strong alkali solution, where the high pH (≈11) of the resulting mixture drives the precipitation of the LDH.[25,36,37] This method has been successfully used for the synthesis of LDHs with a wide variety of chemical compositions, such as Mg^{2+}, Ca^{2+}, Ni^{2+}, Co^{2+}, Cu^{2+}, Zn^{2+}, and Cd^{2+} for the divalent cation (M^{2+}); Al^{3+}, Fe^{3+}, Ga^{3+}, Sn^{3+}, Sc^{3+}, V^{3+}, Cr^{3+}, In^{3+}, and Co^{3+} for the trivalent cation (M^{3+}); and Cl^-, CO_3^{2-}, NO_3^-, OH^-, $Fe(CN)_6^{4-}$, CrO_4^{2-}, and SO_4^{2-} for the interlayer anion (A^{n-}).[14,25−27,36−41] The main limitations of this method are (i) the precipitation of additional (and less soluble) compounds such as hydroxides and carbonates,[20,42−46] (ii) the incorporation of unwanted cations from the strong alkali solution into the LDH structure,[46] and (iii) the environmental impact associated with the use of a strong alkali (i.e., NaOH).[47,48] Moreover, some authors have reported that the coprecipitation method yields less crystalline LDHs than other methods,[31,48−51] which has been suggested to be a direct consequence of an inappropriate solution molar ratio (SMR) of cations during synthesis.[50] Hydrothermal treatment is oftentimes used to increase LDH purity and crystallinity by means of an induced phase change at high temperature and pressure,[30,46,49−52] though this practice leads to additional energy requirements for the synthesis method.

Another synthesis route shown to produce highly crystalline LDHs is the so-called "urea method," where the high pH environment (pH ≈ 9) needed for LDH precipitation is achieved via in situ hydrolysis of urea ($CO(NH_2)_2$) instead of titration with a strong alkali solution.[53] This method has been successfully applied to synthesize certain LDHs, such as those consisting of Mg^{2+}, Ni^{2+}, and Zn^{2+} as the divalent cation; Al^{3+}, Cr^{3+}, and Co^{3+} as the trivalent cation; and Cl^-, CO_3^{2-}, CNO^-, and OH^- as the interlayer anion.[52−56] Nonetheless, limitations of this method include that (i) it is not applicable for LDHs that require higher pH values for precipitation (such as Ca-based LDHs), (ii) it does not solve the issue of undesired precipitation of less soluble compounds, and (iii) it requires an additional ion-exchange if an anion other than CO_3^{2-} is desired in the interlayer space.[55−57] Moreover, the crystallinity of the LDHs is highly dependent on the reaction temperature, requiring near-boiling conditions to obtain crystalline samples in 24−36 h.[53] Some authors have also been able to synthesize LDHs via a sol−gel precipitation, where the hydrolysis of metalorganic precursors gives rise to the precipitation of LDHs.[31,58−60] However, these precursors do not offer any significant benefits to the urea method in terms of crystallinity and purity and are associated with higher CO_2 emissions due to the need to synthesize the metalorganic precursors.[47]

Recently, a modified coprecipitation method has been reported for the synthesis of Ca-based LDHs, whereby the strong alkali and the calcium salt solutions are replaced with a $Ca(OH)_{2(aq)}$ suspension.[47,61] The high pH from the hydrolysis of $Ca(OH)_2$ (pH ≈ 12.5) enables the precipitation of the Ca-LDHs without the need of NaOH. However, it remains to be determined how the concentration of the precursors affects the LDH purity and crystallinity, particularly if it is possible to avoid the formation of less soluble carbonate and hydroxide phases. In general, the main roadblock associated with attainment of phase-pure Ca-based LDHs is the lack of understanding of their formation mechanisms, and how the selected synthesis conditions such as precursor solution compositions affect these mechanisms.

Here, we perform a comprehensive speciation analysis for the synthesis of $Ca_2Fe(OH)_6Cl\cdot 2H_2O$ using the above-mentioned modified coprecipitation method and discuss the effect of Ca/Fe(III) SMR ($SMR_{Ca/Fe}$) on sample purity and crystallinity from an experimental and theoretical point of view. Fe(III) was selected as the trivalent substituent due to its low

https://doi.org/10.1021/acs.cgd.3c00441
Cryst. Growth Des. 2024, 24, 56−70

cost and the ability of monitoring its location and speciation state by the intensity of the orange hue. The formation mechanism of the LDH is elucidated from (i) the available species in solution at the pH of precipitation, (ii) the pH and chemical composition of the supernatant solution after filtration, and (iii) the chemical composition of the precipitated sample, at different Ca/Fe SMRs. Based on this insight, we introduce a new simplified synthesis method for Ca-LDHs of different chemistries, which consists of a one-pot reaction and the in situ hydrolysis of $Ca(OH)_2$. Characterization of the samples using thermogravimetric analysis (TGA) coupled with gas Fourier transform infrared spectroscopy (gas-FTIR), high-resolution X-ray diffraction (HR-XRD), and pair distribution function analysis (PDF) provides evidence of high purity and crystallinity for samples synthesized with a $SMR_{Ca/Fe} \approx 3$.

2. MATERIALS AND METHODS

2.1. Synthesis. *2.1.1. Modified Coprecipitation Method.* To assess the impact of $SMR_{Ca/Fe}$ on the phase purity of $Ca_2Fe(OH)_6Cl{\cdot}2H_2O$, five LDH samples were synthesized in an inert (N_2) environment using different $SMR_{Ca/Fe}$ ratios (1, 2, 3, 5, and 10), based on the synthesis method proposed by Kim et al.[61] Five suspensions of $Ca(OH)_2$ 0.2 M_{eq} ($S_{Ca}1$, $S_{Ca}2$, $S_{Ca}3$, $S_{Ca}5$, $S_{Ca}10$) were each prepared by adding 1.12 g of CaO (ReagentPlus, 99.9% trace metals basis—Sigma-Aldrich) to 100 mL deionized water (18.2 MΩ cm) and mixed for 30 min using a magnetic stirrer bar. A $FeCl_3$ 0.1 M solution was prepared by dissolving 6.76 g of $FeCl_3{\cdot}6H_2O$ (Reag. Ph. Eur., ≥99%—Sigma-Aldrich) in 250 mL of deionized water. Different volumes (100, 50, 33, 20, 10 mL) of $FeCl_3$ 0.1 M were then added to each $Ca(OH)_2$ suspension in a dropwise manner at a rate of 0.5−1.0 mL/min to form 5 solutions with Ca/Fe ratios = 1, 2, 3, 5, and 10 (referred to as S1, S2, S3, S5, and S10 hereafter, see Table 1). After 1 h of additional reaction time, the solids were separated by centrifugation for 1 h at 5000 rpm and, subsequently, dried on a hot plate at 60 °C for 24 h. The pH and color of the supernatant solutions were recorded. Once dried, the solid samples were finely ground with a pestle and mortar (≈1 min) and stored in air-tight containers. This synthesis method was carried out inside a glove box under N_2 flow to prevent early carbonation of the samples.

2.1.2. New Synthesis Method. Precipitation of phase-pure $Ca_2Fe(OH)_6Cl{\cdot}2H_2O$ was performed by adding 0.550 ± 0.001 g of $FeCl_{3(s)}$ (anhydrous ≥99.99% tmb—Sigma-Aldrich) to 50 mL of deionized water (18.2 MΩ cm) until full dissolution, followed by 0.607 ± 0.001 g of $CaO_{(s)}$ (ReagentPlus 99.9% trace metals basis (tmb)—Sigma-Aldrich), aiming for a $SMR_{Ca/Fe} = 3$. The reactor was immediately closed to prevent early carbonation and placed on a magnetic stirrer plate (set at 600 rpm) for 48 h at room temperature (≈20 °C). The final suspension was filtered using vacuum and Whatman Q2 filter paper inside a glove box under N_2 flow. The solids were left to dry at room temperature for 24 h in an inert (N_2) environment, then finely ground with a pestle and mortar (≈1 min) and stored in air-tight containers.

2.2. Characterization. X-ray total scattering measurements were performed on the beamline 11-ID-B at the Advanced Photon Source (APS), Argonne National Laboratory, using a PerkinElmer amorphous silicon 2D image plate detector[62] and a wavelength of 0.2115 Å. Data were acquired using a scan time of 120 s with a sample-to-detector distance of 1000 mm (for diffraction patterns) and 180 mm (for pair distribution function analysis). The 2D data were converted to 1D using GSAS-II with CeO_2 as calibrant.[63] PDFgetX2[64] was used to calculate the pair distribution functions [PDF, $G(r)$], using a $Q_{max} = 22.7$ Å^{-1}.

High-resolution powder X-ray diffraction (XRD) of the phase pure sample was obtained on the beamline ID-22 at the European Synchrotron Radiation Facility, using a 9-channel Si 111 multianalyser stage[65] and a wavelength of 0.2004 Å. Data were acquired using a scan time of 15 s with a sample-to-detector distance of 376 mm.

Thermogravimetric analysis coupled with gas Fourier transform infrared spectroscopy (TGA−FTIR) was performed with a PerkinElmer Pyris 1 TGA and a PerkinElmer Frontier FTIR, where the gases released from the sample during heating with the TGA were conveyed to the FTIR gas cell using a TL8000 transfer line. The TGA−FTIR measurements were performed using N_2 as the sample and balance purge gas for the TGA, and the FTIR instrument and gas cell were also continually purged with N_2 to avoid signal from atmospheric H_2O and CO_2. The IR gas cell and TL8000 transfer line were set at 250 and 300 °C, respectively, and a flow rate of 20 mL/min was employed to transfer the evolved gases from the TGA sample to the FTIR. Single FTIR scans were conducted every 30 s over a wavenumber range of 4000 to 450 cm^{-1}. The TGA temperature program consisted of a 10 min isothermal step at 30 °C and a subsequent ramp to 800 °C at 10 °C/min. The TGA data of samples containing both LDH and $Ca(OH)_2$ were analyzed with a model-fitting approach for a non-isothermal decomposition, as explained elsewhere,[66] with a first order dependency on the reactants composition (expressed in eq 1) for the desorption of adsorbed water, interlayer water, and chemisorbed CO_2, and a second order dependency for the dehydroxylation events in LDHs and $Ca(OH)_2$ (expressed in eq 2) to account for the involvement of two neighboring hydroxyl units that subsequently form a H_2O molecule.

$$\frac{d\alpha_i(T)}{dT} = \frac{k_{o_i} e^{-E_i^o/RT}}{\beta}[1 - \alpha_i(T)] \quad (1)$$

$$\frac{d\alpha_i(T)}{dT} = \frac{k_{o_i} e^{-E_i^o/RT}}{\beta}[1 - \alpha_i(T)]^2 \quad (2)$$

Surface morphology of the samples was studied with scanning electron microscopy (SEM) using a FEI/Phillips XL30 FEG-SEM. Powder samples were mounted on a SEM holder using double sided carbon tape and SEM scans were performed with a 5 keV beam in an ultra-high vacuum chamber.

3. RESULTS AND DISCUSSION

The first part of the Results and Discussion focuses on the speciation analysis of CaO and $FeCl_3$ in water, where the aqueous species that are prevalent and necessary for the formation of $Ca_2Fe(OH)_6Cl{\cdot}2H_2O$ during the coprecipitation reaction are identified and discussed. This new insight is used to explain the pH evolution during the dropwise coprecipitation reaction that has been previously reported in the literature.[61] The second part of the Results and Discussion presents experimental data on the impact of starting $SMR_{Ca/Fe}$ on formation of $Ca_2Fe(OH)_6Cl{\cdot}2H_2O$ and secondary phases. A new formation mechanism for $Ca_2Fe(OH)_6Cl{\cdot}2H_2O$ is discussed and used to determine the ideal $SMR_{Ca/Fe}$ needed to obtain phase-pure $Ca_2Fe(OH)_6Cl{\cdot}2H_2O$. Finally, a simplified coprecipitation green synthesis approach to obtain phase-pure $Ca_2Fe(OH)_6Cl{\cdot}2H_2O$ is outlined that negates the need for dropwise mixing or the use of an inert environment.

3.1. Theoretical Speciation Analysis. *3.1.1. Ca(II) in Aqueous Solution.* It is well documented that the dissolution of CaO in water yields an alkaline solution, governed by the reactions presented in eqs 3−6.[67]

$$CaO_{(s)} + H_2O \rightarrow Ca(OH)_{2(s)} \quad (3)$$

$$Ca(OH)_{2(aq)} \overset{K_{b1[Ca(OH)_2]}}{\rightleftharpoons} CaOH^+_{(aq)} + OH^-_{(aq)} \quad (4)$$

$$CaOH^+_{(aq)} \overset{K_{b2[Ca(OH)_2]}}{\rightleftharpoons} Ca^{2+}_{(aq)} + OH^-_{(aq)} \quad (5)$$

https://doi.org/10.1021/acs.cgd.3c00441
Cryst. Growth Des. 2024, 24, 56−70

$$Ca(OH)_{2(s)} \overset{K_{SP[Ca(OH)_2]}}{\rightleftharpoons} Ca^{2+}_{(aq)} + 2OH^{-}_{(aq)} \quad (6)$$

where the concentration of the different Ca(II) species in solution depends on the equilibrium constants $K_{bi[Ca(OH)_2]}$ and solubility product $K_{SP[Ca(OH)_2]}$, as defined in eqs 7−9 for an ideal solution under standard conditions.[68]

$$K_{b1[Ca(OH)_2]} = \frac{[CaOH^{+}_{(aq)}][OH^{-}_{(aq)}]}{[Ca(OH)_{2(aq)}]} = 0.010 \quad (7)$$

$$K_{b2[Ca(OH)_2]} = \frac{[Ca^{2+}_{(aq)}][OH^{-}_{(aq)}]}{[CaOH^{+}_{(aq)}]} = 0.071 \quad (8)$$

$$K_{SP[Ca(OH)_2]} = [Ca^{2+}_{(aq)}]_{(sat)}[OH^{-}_{(aq)}]^2_{(sat)} = 4.5 \times 10^{-6} \quad (9)$$

The presence of $Ca(OH)_{2(aq)}$ has only been addressed recently[67,68] and there is a lack of consensus on the values of these constants, which have been reported to be between 0.01 and 0.32 for $K_{b1[Ca(OH)_2]}$,[67,68] 0.03 and 0.67 for $K_{b2[Ca(OH)_2]}$[67,69−74] and (4.5−88) × 10^{-6} for $K_{SP[Ca(OH)_2]}$.[67,70] Here, we make use of the values reported by Lito et al.[68] on the basis that (i) they take into consideration the presence of $Ca(OH)_{2(aq)}$ species, (ii) their $K_{b2[Ca(OH)_2]}$ value is in good agreement with previous studies,[75−77] and (iii) their $K_{SP[Ca(OH)_2]}$ value is supported by the observations made in this study on the solubility of $Ca(OH)_2$. The speciation analysis of a Ca(II) 0.01 M solution with respect to pH for an ideal solution under standard conditions is represented in Figure 1, where it can be seen that $Ca^{2+}_{(aq)}$ is the most abundant

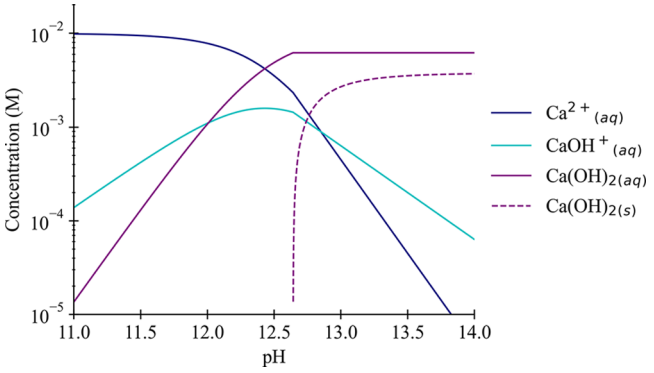

Figure 1. Speciation of Ca(II) 0.01 M in aqueous solution at 25 °C as a function of pH, with $K_{b1[Ca(OH)_2]} = 0.010$, $K_{b2[Ca(OH)_2]} = 0.071$, and $K_{SP[Ca(OH)_2]} = 4.5 \times 10^{-6}$.

species up until a pH of 12.4, after which $Ca(OH)_{2(aq)}$ starts to dominate until the precipitation conditions are met (pH = 12.6), and the concentration of $Ca(OH)_{2(s)}$ starts to increase at the expense of the ionic species. In other words, the speciation analysis of Ca(II) indicates that no precipitated $Ca(OH)_2$ would remain in equilibrium at a pH < 12.6. Moreover, if a secondary reaction were to consume OH^-, the dissolution of $Ca(OH)_{2(s)}$ would act as a buffer around this pH threshold following Le Chatelier's principle. Equation 9 also shows that as $[Ca(II)]_{tot}$ increases, the threshold value for the precipitation pH must decrease. For $[Ca(II)]_{tot}$ = 0.2 M (as presented in Section 2.1), the threshold occurs at pH ≈ 11.7.

3.1.2. Fe(III) in Aqueous Solution. Contrary to CaO, $FeCl_3$ yields an acidic solution when dissolved in water, which can be described by the equilibrium reactions presented in eqs 10−14[78−81]

$$FeCl_{3(s)} \xrightarrow{H_2O} Fe^{3+}_{(aq)} + 3Cl^{-}_{(aq)} \quad (10)$$

$$Fe^{3+}_{(aq)} + H_2O \overset{K_{1[Fe^{3+}]}}{\rightleftharpoons} FeOH^{2+}_{(aq)} + H^{+}_{(aq)} \quad (11)$$

$$Fe^{3+}_{(aq)} + 2H_2O \overset{K_{2[Fe^{3+}]}}{\rightleftharpoons} Fe(OH)^{+}_{2(aq)} + 2H^{+}_{(aq)} \quad (12)$$

$$Fe^{3+}_{(aq)} + 3H_2O \overset{K_{3[Fe^{3+}]}}{\rightleftharpoons} Fe(OH)_{3(aq)} + 3H^{+}_{(aq)} \quad (13)$$

$$Fe^{3+}_{(aq)} + 4H_2O \overset{K_{4[Fe^{3+}]}}{\rightleftharpoons} Fe(OH)^{-}_{4(aq)} + 4H^{+}_{(aq)} \quad (14)$$

where the concentrations of the different Fe(III) species in solution depend on the equilibrium constants $K_{i[Fe^{3+}]}$, as defined in eqs 15−18 for an ideal solution under standard conditions.[79]

$$K_{1[Fe^{3+}]} = \frac{[FeOH^{2+}_{(aq)}][H^{+}_{(aq)}]}{[Fe^{3+}_{(aq)}]} = 6.5 \times 10^{-3} \quad (15)$$

$$K_{2[Fe^{3+}]} = \frac{[Fe(OH)^{+}_{2(aq)}][H^{+}_{(aq)}]^2}{[Fe^{3+}_{(aq)}]} = 2.1 \times 10^{-6} \quad (16)$$

$$K_{3[Fe^{3+}]} = \frac{[Fe(OH)_{3(aq)}][H^{+}_{(aq)}]^3}{[Fe^{3+}_{(aq)}]} = 5.0 \times 10^{-15} \quad (17)$$

$$K_{4[Fe^{3+}]} = \frac{[Fe(OH)^{-}_{4(aq)}][H^{+}_{(aq)}]^4}{[Fe^{3+}_{(aq)}]} = 1.9 \times 10^{-22} \quad (18)$$

Studies on the speciation analysis of Fe(III) tend to focus on the aqueous system (below the saturation limit).[78−80] As such, the concentrations of the Fe(III) species as a function of pH can be represented as displayed in Figure 2a, where at pH > 8, the main species in solution is $Fe(OH)^{-}_{4(aq)}$. However, this representation is only valid for very dilute concentrations ($[Fe(III)]_{tot}$ < 1.5 × 10^{-10} M). For more concentrated solutions, as is the case for Ca-based LDH synthesis, the precipitation of $Fe(OH)_3$ must also be considered. The solubility product constant of 2-line ferrihydrite (the ferric hydroxide phase detected in this investigation) has been reported to be $K_{SP[Fe(OH)_3]} \approx 1 \times 10^{-39}$ for the equilibrium reaction presented in eq 19.[78]

$$Fe(OH)_{3(s)} \overset{K_{SP[Fe(OH)_3]}}{\rightleftharpoons} Fe^{3+}_{(aq)} + 3OH^{-}_{(aq)} \quad (19)$$

The speciation analysis of a Fe(III) 0.01 M solution with respect to pH for an ideal solution under standard conditions is represented in Figure 2b, where it can be observed that the most abundant species for pH > 2 is in fact the precipitated ferrihydrite. However, the high relative abundance of $Fe(OH)^{-}_{4(aq)}$ with respect to other Fe(III) aqueous species at pH > 8 remains. Moreover, if we rearrange eq 18 and we

https://doi.org/10.1021/acs.cgd.3c00441
Cryst. Growth Des. 2024, 24, 56−70

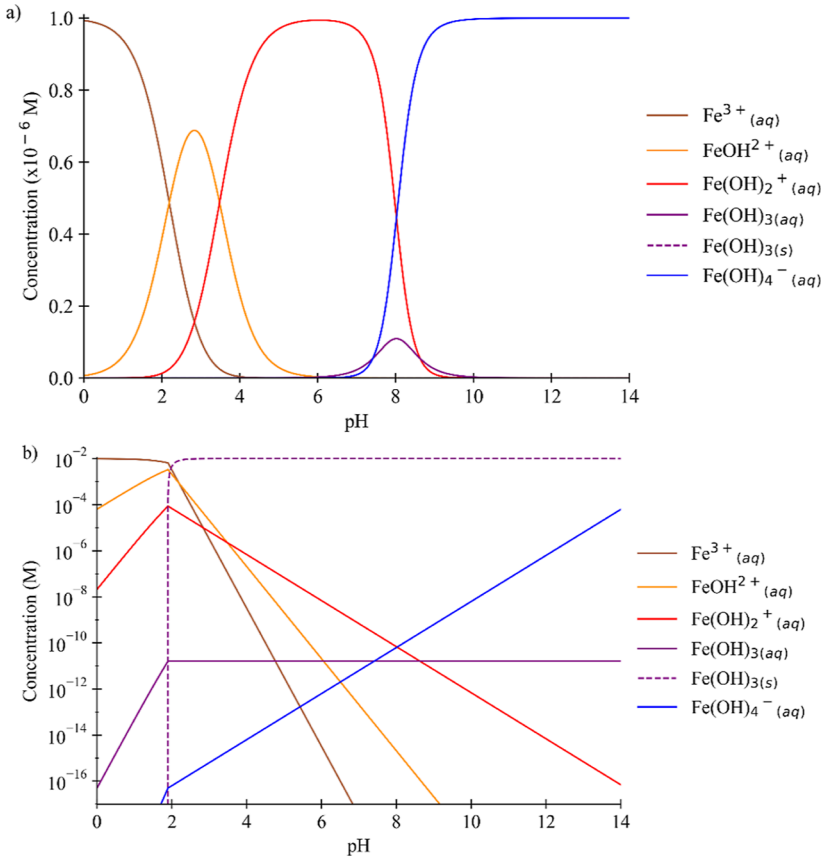

Figure 2. Speciation of Fe(III) as a function of pH for (a) $[Fe(III)]_{tot} = 1 \times 10^{-10}$ M and (b) $[Fe(III)]_{tot} = 0.01$ M, according to hydrolysis constants $K_{1[Fe^{3+}]} = 6.5 \times 10^{-3}$, $K_{2[Fe^{3+}]} = 2.1 \times 10^{-6}$, $K_{3[Fe^{3+}]} = 5.0 \times 10^{-15}$ and $K_{4[Fe^{3+}]} = 1.9 \times 10^{-22}$.[79] Note that concentration in (a) is given on a linear axis while (b) is logarithmic.

assume saturation conditions for the dissolution of ferrihydrite, it can be shown that the concentration of the tetrahydroxylated ion depends only on the pH (eqs 20–24). This also means that for any pH, the concentration of tetrahydroxylated iron will always be lower than $1.9 \times 10^{pH-19}$ M, as expressed in eq 25, irrespective of $[Fe(III)]_{tot}$.

$$[Fe(OH)_{4(aq)}^{-}] = K_{4[Fe^{3+}]}\frac{[Fe_{(aq)}^{3+}]}{[H_{(aq)}^{+}]^4} \tag{20}$$

$$[Fe_{(aq)}^{3+}] = \frac{K_{SP[Fe(OH)_3]}}{[OH_{(aq)}^{-}]^3} \tag{21}$$

$$[Fe(OH)_{4(aq)}^{-}]_{sat} = K_{4[Fe^{3+}]}\frac{K_{SP[Fe(OH)_3]}}{[H_{(aq)}^{+}]^4[OH_{(aq)}^{-}]^3} \tag{22}$$

$$[Fe(OH)_{4(aq)}^{-}]_{sat} = \frac{K_{4[Fe^{3+}]}K_{SP[Fe(OH)_3]}}{K_W{}^3}\frac{1}{[H_{(aq)}^{+}]} \tag{23}$$

$$[Fe(OH)_{4(aq)}^{-}]_{sat} = 1.9 \times 10^{pH-19} \tag{24}$$

$$[Fe(OH)_{4(aq)}^{-}] < 1.9 \times 10^{pH-19} \tag{25}$$

A similar approach can be taken with the other Fe(III) species, yielding the relations presented in eqs 26–28.

$$[Fe(OH)_{3(aq)}]_{(sat)} = \frac{K_{3[Fe^{3+}]}K_{SP[Fe(OH)_3]}}{K_W{}^3} = 5.0 \times 10^{-12} \tag{26}$$

$$[Fe(OH)_{2(aq)}^{+}]_{(sat)} = \frac{K_{2[Fe^{3+}]}K_{SP[Fe(OH)_3]}}{K_W{}^3}[H_{(aq)}^{+}] = 2.1 \times 10^{-3-pH} \tag{27}$$

$$[FeOH_{(aq)}^{2+}]_{(sat)} = \frac{K_{1[Fe^{3+}]}K_{SP[Fe(OH)_3]}}{K_W{}^3}[H_{(aq)}^{+}]^2 = 6.5 \times 10^{-2pH} \tag{28}$$

According to the relationships presented in eqs 24–28, $Fe(OH)_{4(aq)}^{-}$ starts to dominate the composition of the Fe(III) species in solution at pH > 8, reaching a value of 6×10^{-7} M at pH = 12.5. This finding, along with the higher concentration of LDH in samples precipitated at higher pH found by Kim et al.[61] and corroborated by this study (see Section 3.2), suggests that the Fe(III) species taking part in the formation of $Ca_2Fe(OH)_6Cl{\cdot}2H_2O$ is in fact $Fe(OH)_{4(aq)}^{-}$. This means that before the precipitation of $Ca_2Fe(OH)_6Cl{\cdot}2H_2O$ can occur, the Fe^{3+} added to the reactor needs to undergo several hydroxylation steps, consuming hydroxyls in the process. As shown in Section 3.1.1, this consumption of OH^- causes the dissolution of sufficient amounts of solid $Ca(OH)_2$ to maintain the equilibrium described by eq 9, thereby maintaining the pH at ≈12.6 for $[Ca(II)]_{tot} = 0.01$ M and at ≈11.7 for $[Ca(II)]_{tot}$

https://doi.org/10.1021/acs.cgd.3c00441
Cryst. Growth Des. 2024, 24, 56−70

= 0.2 M. This buffering effect ends upon complete dissolution of the solid $Ca(OH)_2$, after which the pH of the solution starts decreasing if further OH^- is consumed.

3.1.3. Analysis of pH Fluctuations during the Precipitation of $Ca_2Fe(OH)_6Cl{\cdot}2H_2O$. The above speciation analysis can be used to provide additional insights on the formation mechanism $Ca_2Fe(OH)_6Cl{\cdot}2H_2O$ when synthesized using the coprecipitation dropwise approach, as utilized by Kim et al.[61] However, contrary to the claims of Kim et al. that the formation of the LDH by means of the titration of $Ca(OH)_2$ with $FeCl_{3(aq)}$ occurs via post-isomorphic substitution, the speciation analysis supports a dissolution−precipitation formation mechanism to explain the pH changes reproduced in Figure 3. This claim can be supported by considering the

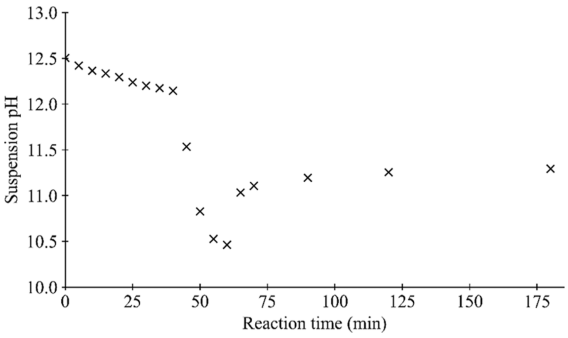

Figure 3. Suspension pH monitored during addition of $FeCl_3$ 0.1 M to 100 mL of $Ca(OH)_{2(s)}$ 0.2 M_{eq} suspension at a flow rate of 0.8 mL/min.[61]

conditions of the synthesis method, where a dropping rate of $0.8\frac{\text{mL } FeCl_3\ 0.1\ M}{\text{min}}$ to 100 mL of a $Ca(OH)_2$ suspension of pH(t = 0) = 12.5 would yield a total concentration of iron species $[Fe(III)]_{tot} = 1.3 \times 10^{-5}$ M within 1 s of mixing, significantly above the 1.5×10^{-10} M saturation limit of $Fe(OH)_{3(s)}$, as shown in Section 3.1.2. Therefore, the synthesis of the LDH takes place at saturated conditions for $Fe(OH)_{3(s)}$, and the initial concentrations of the Fe(III) species in solution can be obtained by applying eqs 24−28. Given that the $Ca(OH)_2$ suspension acts as a buffer around pH = 12, it can be seen from Figure 2b that $[Fe(OH)^+_{2(aq)}]$ and $[FeOH^{2+}_{(aq)}]$ are negligible (and, thus, so are their changes), $[Fe(OH)_{3(aq)}]$ remains constant at 5.0×10^{-12} M, and $[Fe(OH)^-_{4(aq)}]$ decreases from 6×10^{-7} M with decreasing pH (see Figure 2b). As such the first decrease in pH as $FeCl_3$ 0.1 M is added to the $Ca(OH)_2$ suspension is due to the precipitation of ferrihydrite ($Fe(OH)_{3(s)}$). The competing precipitation of $Ca_2Fe(OH)_6Cl{\cdot}2H_2O$ could also be partially responsible for this decrease in pH, as it would promote the dissolution of $Fe(OH)_{3(s)}$ into $Fe(OH)^-_{4(aq)}$, following Le Chatelier's principle. However, the relative contributions are still unknown. The observations made during synthesis (presented later in Section 3.2.1) indicate that the precipitation of $Fe(OH)_{3(s)}$ is almost instantaneous at t = 0 s, and that the conversion rate to $Ca_2Fe(OH)_6Cl{\cdot}2H_2O$ is significantly slower.

As mentioned in Section 3.1.2, the precipitation of ferrihydrite upon dropwise addition of $FeCl_{3(aq)}$ to the $Ca(OH)_2$ suspension leads to the consumption of hydroxyl groups, causing the dissolution of $Ca(OH)_{2(s)}$ following Le Chatelier's principle. At the same time, the consumption of $Fe(OH)^-_{4(aq)}$ due to the precipitation of $Ca_2Fe(OH)_6Cl{\cdot}2H_2O$ also reduces the pH via the redissolution of $Fe(OH)_{3(s)}$ and replenishment of $Fe(OH)^-_{4(aq)}$ to maintain its saturation condition. This consumption of OH^- to form $Fe(OH)^-_{4(aq)}$ is initially buffered by the dissolution of $Ca(OH)_{2(s)}$, yielding a mild decrease in pH. Once all the $Ca(OH)_{2(s)}$ is consumed, the buffer effect ends and further addition of $FeCl_{3(aq)}$ causes an abrupt decrease in pH. This sudden decrease in pH is visible in Figure 3 at t = 40 min.

It is worth mentioning that, at the precipitation pH of LDH observed in this study (≥11), the main species in solution are $Fe(OH)^-_4$, Ca^{2+} [$Ca(OH)_{2(aq)}$ for pH > 12.4], Cl^-, and OH^- (see Figures 1 and 2b), thus it is hypothesized that the general equation of the precipitation step can be described as (eq 29)

$$2Ca^{2+}_{(aq)} + 2OH^-_{(aq)} + Fe(OH)^-_{4(aq)} + Cl^-_{(aq)} + 2H_2O \overset{K_{SP}[LDH]}{\rightleftharpoons} Ca_2Fe(OH)_6Cl{\cdot}2H_2O_{(s)} \quad (29)$$

where K_{SP}[LDH] is the solubility product constant of the LDH. It follows that the solubility product quotient Q_{SP}[LDH], defined here as $[Ca^{2+}_{(aq)}]^2[Fe(OH)^-_{4(aq)}][(OH)^-_{(aq)}]^2[Cl^-_{(aq)}]$, is a function of $K_{i[Fe^{3+}]}$, $K_{SP[Fe(OH)_3]}$, $K_{bi[Ca(OH)_2]}$, $K_{SP[Ca(OH)_2]}$, $[Fe(III)]_{tot}$, and $[Ca(II)]_{tot}$. Further work is needed to define this function for the solubility product quotient as well as K_{SP}[LDH], however, eq 29 shows that the precipitation of $Ca_2Fe(OH)_6Cl{\cdot}2H_2O_{(s)}$ consumes equal amounts of Ca^{2+} and OH^-. Hence, once all the $Ca(OH)_{2(s)}$ is consumed, the precipitation of the LDH contributes further to the decrease in pH.

In summary, the abrupt pH decrease observed by Kim. et al.[61] can be explained by a dissolution−precipitation route, as the pH of the $Ca(OH)_2$ 0.2 M suspension (pH = 12.5[61]) is in fact expected to drop upon titration with the $FeCl_3$ 0.1 M, first slowly due to the buffer effect of $Ca(OH)_{2(s)}$, and then abruptly once all the $Ca(OH)_{2(s)}$ has dissolved. The increase in pH observed after the end point of $FeCl_{3(aq)}$ addition can be explained by a kinetic effect, where the additional $FeCl_{3(aq)}$ acidifies the solution causing the delayed redissolution of LDH to preserve the thermodynamic equilibrium presented in eq 29.

3.1.4. Calculation of $SMR_{Ca/Fe}$ to Obtain Pure $Ca_2Fe(OH)_6Cl{\cdot}2H_2O$. In Section 3.1.3, we showed that precipitated $Ca(OH)_{2(s)}$ buffers the solution at a pH between 11.7 and 12.5 during the synthesis of $Ca_2Fe(OH)_6Cl{\cdot}2H_2O$. We have also seen experimentally that high purity is not achieved when the solution pH drops below 11 due to the coprecipitation of ferrihydrite (see Section 3.2.2). This means that, to achieve sample purity, we need to ensure a solution pH high enough to prevent the precipitation of ferrihydrite but below the saturation point of portlandite. Experimental results show

https://doi.org/10.1021/acs.cgd.3c00441
Cryst. Growth Des. 2024, 24, 56−70

that phase-pure $Ca_2Fe(OH)_6Cl{\cdot}2H_2O$ can be obtained from solutions with final pH = 12 (± 0.5). In this section, we explain how to calculate the amount of reagents needed to obtain phase-pure $Ca_2Fe(OH)_6Cl{\cdot}2H_2O$.

We begin by assuming a final solution pH = 12, to avoid the coprecipitation of both ferrihydrite and portlandite. Then we need to determine which will be the limiting reagent. As we showed in Section 3.1.2, for an undersaturated solution of $Fe(OH)_3$ with a pH = 12, we can approximate the total concentration of iron species ($[Fe(III)]_{tot}$) with the concentration of the tetrahydroxylated species ($[Fe(OH)_4^-]_{(aq)}$), which must be lower than its concentration in a saturated solution, as expressed by eq 30. Hence, the total concentration of Fe(III) species in solution after the complete dissolution of the solid ferrihydrite must be lower than 1.9×10^{-7} M.

$$[Fe(III)]_{tot} \approx [Fe(OH)_4^-]_{(aq)} < [Fe(OH)_4^-]_{(sat)} \quad (30)$$

$$[Fe(III)]_{tot} < 1.9 \times 10^{-7}\ M \quad (31)$$

A similar approximation can be made for the Ca(II) system, were the dominant species at pH = 12 is Ca^{2+} (as discussed in Section 3.1.1) and its concentration in a saturated solution can be calculated by rearranging eq 9

$$[Ca^{2+}]_{(sat)} = 10^{-2pH}\frac{K_{SP[Ca(OH)_2]}}{{K_w}^2} \quad (32)$$

$$[Ca^{2+}]_{(sat)} = 4.5 \times 10^{-2}\ M \quad (33)$$

Given that we are aiming at being just below the saturation pH for portlandite, we anticipate $[Ca(II)]_{tot} \approx [Ca^{2+}]_{(sat)}$. In other words, at a pH = 12 $[Ca(II)]_{tot} \gg [Fe(III)]_{tot}$, deeming $FeCl_3$ as the limiting reagent.

Now we need to describe the general equation for the overall chemical reaction, which can be done by adding and balancing eqs 3, 6, 10, 14, and 29

$$3CaO_{(s)} + 3H_2O \rightarrow 3Ca(OH)_{2(s)} \quad (3)$$

$$3Ca(OH)_{2(s)} \rightarrow 3Ca^{2+}{}_{(aq)} + 6OH^-_{(aq)} \quad (6)$$

$$FeCl_{3(s)} \rightarrow Fe^{3+}_{(aq)} + 3Cl^-_{(aq)} \quad (10)$$

$$Fe^{3+}_{(aq)} + 4OH^- \rightarrow Fe(OH)_{4(aq)}^- \quad (14)$$

$$2Ca^{2+}_{(aq)} + 2(OH)^-_{(aq)} + Fe(OH)_{4(aq)}^- + Cl^-_{(aq)} + 2H_2O \xrightarrow{pH=12} Ca_2Fe(OH)_6Cl{\cdot}2H_2O_{(s)} \quad (29)$$

$$FeCl_{3(s)} + 3CaO_{(s)} + 5H_2O \xrightarrow{pH=12} Ca_2Fe(OH)_6Cl{\cdot}2H_2O_{(s)} + 2Cl^-_{(aq)} + Ca^{2+}_{(aq)} \quad (34)$$

Equation 34 is the general equation that describes the precipitation of $Ca_2Fe(OH)_6Cl{\cdot}2H_2O$ from the reaction of $FeCl_3$ and CaO in an aqueous solution. It is interesting to see that, although the desired product has a Ca/Fe molar ratio = 2, the initial Ca/Fe solution molar ratio (stoichiometric $SMR_{Ca/Fe}$) is = 3. This is due to the additional number of equivalents (OH^-) needed to precipitate the LDH, which are only provided by the dissolution of CaO in water.

However, the actual $SMR_{Ca/Fe}$ must be >3 because the reaction needs to happen at a pH = 12 to avoid secondary coprecipitation products, which requires additional CaO as it is the concentration of OH^- equivalents in solution what dictates the pH. To obtain a pH = 12, a 0.01 eq/L is needed, which can be obtained from 0.005 M of CaO. Thus, the total amount of CaO (n_{CaO}) needed to achieve full conversion of the $FeCl_3$ (n_{FeCl_3}) without coprecipitating portlandite can be calculated as follows:

$$n_{CaO} = 3 \times n_{FeCl_3} + V(0.005M) \quad (35)$$

$$SMR_{Ca/Fe} = \frac{n_{CaO}}{n_{FeCl_3}} = 3 + V\frac{(0.005\ M)}{n_{FeCl_3}} \quad (36)$$

where V is the volume of the solution, which needs to be high enough to avoid the precipitation of portlandite. As expressed by eq 33, $[Ca^{2+}_{(sat)}]_{(pH=12)} = 4.5 \times 10^{-2}$ M. In order to prevent the coprecipitation of portlandite, $[Ca^{2+}_{(aq)}]_{(pH=12)} < 4.5 \times 10^{-2}$ M. From eq 34, we know that for every mole of LDH that precipitates, a mole of Ca^{2+} is released into the solution, so we can calculate the total amount of Ca(II) in solution using eq 37. Solving the inequality (eq 38) yields the minimum volume V (eq 39) to achieve phase-purity of the LDH.

$$[Ca^{2+}_{(aq)}]_{(pH=12)} = \frac{n_{FeCl_3}}{V} + 0.005\ M \quad (37)$$

$$\frac{n_{FeCl_3}}{V} + 0.005\ M < 0.045\ M \quad (38)$$

$$V > \frac{n_{FeCl_3}}{0.04\ M} \quad (39)$$

This speciation analysis is transferrable to other $CaM^{3+}Cl$ LDHs provided that the appropriate equilibrium constants and solubility products are known for the trivalent cations and other possible precipitates.

3.2. Impact of $SMR_{Ca/Fe}$ on Phase Purity. Five CaFeCl-LDH samples were prepared using the modified coprecipitation method described in Section 2.1.1 with $SMR_{Ca/Fe}$ = 1, 2, 3, 5 and 10 (referred to as S1, S2, S3, S5, and S10 hereafter) and analyzed using XRD, PDF, TGA, and SEM. Table 1 reports the main findings, where observations of the supernatant along with sample purity and the presence of secondary phases are given. These details provide further insights on the reaction mechanism that leads to the precipitation of $Ca_2Fe(OH)_6Cl{\cdot}2H_2O_{(s)}$, as discussed in more detail below. The following subsections discuss the effects of $SMR_{Ca/Fe}$ on phase purity, however it is important to note that the concentrations of the reactant solutions will also influence this behavior. In this study, the concentrations were kept fixed at 0.2 M_{eq} and 0.1 M for $Ca(OH)_2$ and $FeCl_3$, respectively.

3.2.1. Visual Observations during Synthesis and pH Measurements. Upon contact of the $FeCl_{3(aq)}$ solution droplets (translucent bright orange) with the $Ca(OH)_{2(s)}$ suspension (opaque white), a dark red precipitate immediately formed. The dark red particles then seemed to redissolve in the opaque $Ca(OH)_{2(aq)}$ suspension, giving the reaction solution an orange hue. The orange color became stronger with time, as the $[Fe(III)]_{tot}$ increased. Once the addition of $FeCl_{3(aq)}$

https://doi.org/10.1021/acs.cgd.3c00441
Cryst. Growth Des. 2024, 24, 56−70

ended, the solution of S1 remained dark red and its dark red particles remained undissolved. Upon filtration, the pH of the supernatant solution was measured as 2.5, and the dry precipitate was composed of dark and shiny loose particles that could not be broken with a pestle and mortar. These observations are in agreement with the dominance of $Fe(OH)_{3(s)}$ at pH = 2.5 (see Figure 2b), which occurs when $SMR_{Ca/Fe}$ = 1 (see Supporting Information).

Contrary to the visual observations of S1, the initial dark brown precipitate in S3, S5, and S10 (and S2 in a lesser amount) redissolved and was replaced by a light tan precipitate as the solutions became translucent and colorless. It can be inferred from these observations that the $Fe(OH)_{3(s)}$ (dark precipitate) redissolved and the Fe(III) species in solution (responsible for the orange hue[81]) were consumed as the $Ca_2Fe(OH)_6Cl{\cdot}2H_2O$ (white precipitate) formed. Upon filtration, the precipitates of S2, S3, S5, and S10 formed a paste-like substance that was easily ground with pestle and mortar after drying. The final samples were orange (S2), tan (S3), and white (S5 and S10) chalk-like powders. Unlike S3, S5, and S10, which had a translucent supernatant solution with pH > 12, the supernatant solution of S2 had a pH of 11 and remained orange after synthesis, suggesting a high concentration of Fe(III) species in solution. Interestingly, the pH of the supernatant solutions increased with $SMR_{Ca/Fe}$ until $SMR_{Ca/Fe}$ = 3, where the pH was measured to be 12.5 for S3, S5, and S10. This buffer effect is likely caused by the remaining $Ca(OH)_{2(s)}$ at higher $SMR_{Ca/Fe}$.

The observations made during synthesis show that the $SMR_{Ca/Fe}$ has a direct impact on phase purity, so that there is a minimum $SMR_{Ca/Fe}$ value between 1 and 2 (corresponding to pH = 2.5 and 11.5, respectively—see Supporting Information) that drives the precipitation of the LDH, and a stoichiometric value between 2 and 5, below which $Fe(OH)_{3(s)}$ does not fully redissolve and above which $Ca(OH)_{2(s)}$ precipitates. These findings are in agreement with calculations made in Section 3.1.4, where $SMR_{Ca/Fe}$ = 3 was deemed as the stoichiometric value for precipitation of phase-pure $Ca_2Fe(OH)_6Cl{\cdot}2H_2O$.

3.2.2. Characterization of Final Powder Samples. After synthesis, phase purity of the powder samples S1, S2, S3, S5, and S10 was assessed using XRD, PDF analysis, and TGA–FTIR, while SEM was used to determine particle morphology. The XRD patterns and PDFs of S1, S2, S3, S5, and S10 are displayed in Figures 4 and 5, respectively. The TGA weight loss data of S2, S3, S5, and S10 are presented in Figure 6 along with the decomposition curve of portlandite recrystallized from CaO under the same synthesis conditions (equivalent to $SMR_{Ca/Fe}$ = ∞). We applied the model-fitting approach explained in Section 2.2 to the TGA weight loss curves to estimate the purity of samples S3, S5, and S10. The calculated LDH purity and relative amount of different secondary phases are presented in Table 2. The SEM images in Figure 7 show the impact of $SMR_{Ca/Fe}$ on particle size and shape, while the high magnification images in Figure 8 focus on surface morphology.

During synthesis of the S1 sample, a solid precipitated as large and reflective particles of high hardness that subsequently could not be ground into a fine powder, while the collected supernatant was found to be acidic. From SEM analysis, S1 particles are seen to display angular edges (Figure 7f) and relatively smooth surface morphologies with distinguishable

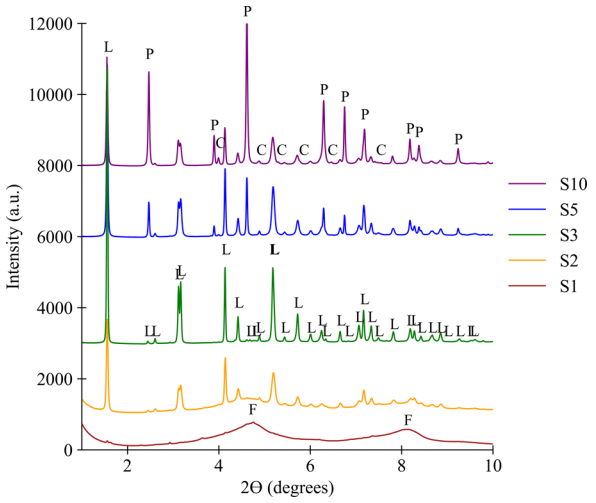

Figure 4. XRD patterns of samples S1, S2, S3, S5, and S10 ($SMR_{Ca/Fe}$ = 1, 2, 3, 5, and 10, respectively) obtained using (λ = 0.2115 Å). F: 2-line ferrihydrite, L: crystalline $Ca_2Fe(OH)_6{\cdot}2H_2O$, P: portlandite, and C: calcite.

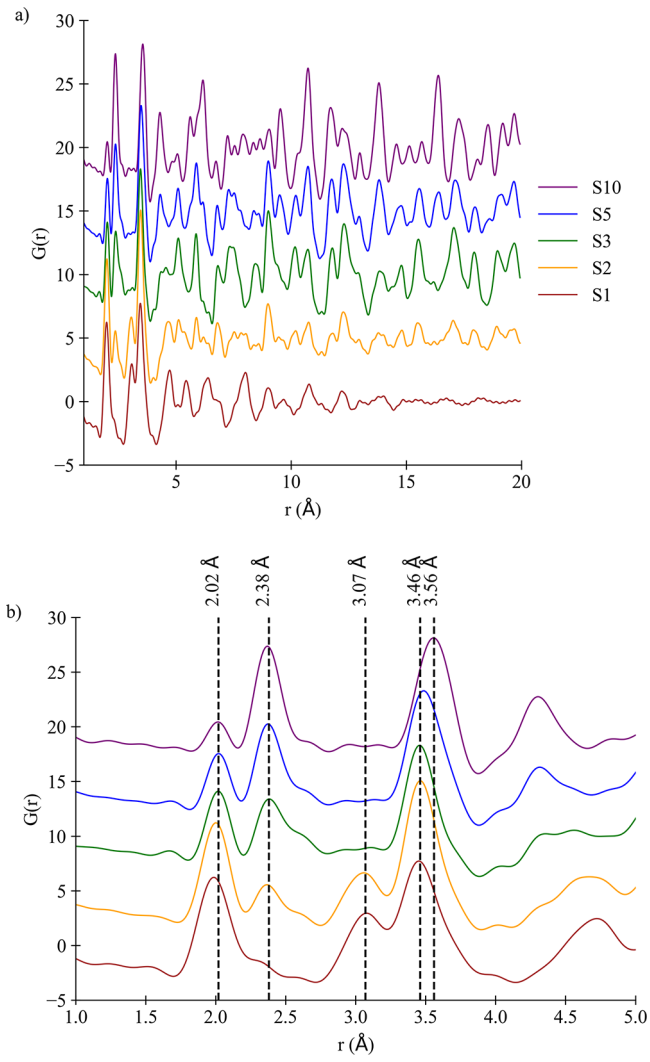

Figure 5. PDF curves of samples S1, S2, S3, S5, and S10 ($SMR_{Ca/Fe}$ = 1, 2, 3, 5, and 10, respectively). (a) Showing long-range atom–atom distances out to 20 Å, and (b) short- and medium-range atom–atom distances out to 5 Å.

https://doi.org/10.1021/acs.cgd.3c00441
Cryst. Growth Des. 2024, 24, 56–70

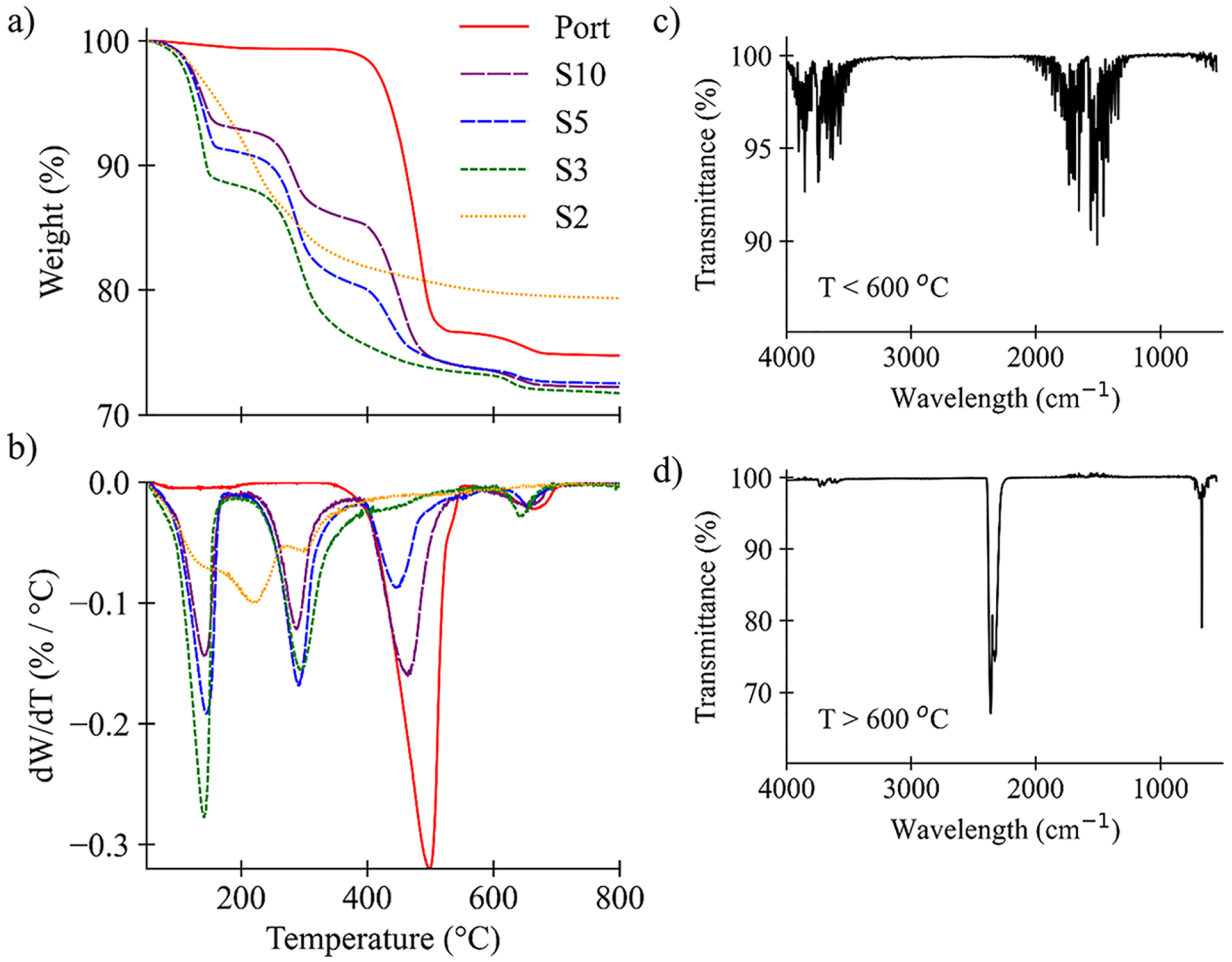

Figure 6. (a) TGA curves of powder samples S2, S3, S5, and S10 ($SMR_{Ca/Fe}$ = 2, 3, 5 and 10, respectively) and (b) their corresponding derivative curves. The decomposition curve of portlandite (recrystallized under the same synthesis conditions) is shown as a reference. The gases released from the TGA sample were monitored using the gas cell mounted on the FTIR instrument. Examples of the recorded FTIR spectra for the dehydroxylation and decarbonation of partially carbonated portlandite are presented in (c,d), respectively.

Table 2. Composition of Samples S3, S5, and S10 Calculated from TGA Using the Model-Fitting Approach[a]

ID	composition from TGA (% m/m, ±2.0%)					
	$H_2O_{(ads)}$	$Ca(OH)_2$	$Ca_2Fe(OH)_6Cl{\cdot}2H_2O$	$CaCO_3$	other	R^2
S10	0.8	46.0	48.0	3.0	2.2	0.999
S5	1.5	24.0	67.0	3.5	4.0	0.999
S3	0.5	1.5	91.0	2.0	5.0	0.997

[a]Fits are reported in the Supporting Information. Phases not included in the model are aggregated under "other."

step-like features at a length scale below a micron (Figure 8f). The XRD pattern of S1 (Figure 4) shows two diffuse peaks centered at 2θ of ~4.7 and ~8.1° (using λ = 0.2115 Å), similar to that of amorphous 2-line ferrihydrite.[81] PDF analysis agrees with this phase assignment, specifically by the amorphous nature of the PDF curve (atomic ordering out to 15 Å) and peaks characteristic of this phase at 2.00 (Fe−O bond), 3.07 (first Fe−Fe correlation with contributions from O−O), and 3.46 Å (second Fe−Fe correlation with contributions from Fe−O)[82] (Figure 5). This finding of pure amorphous ferrihydrite in S1 provides further evidence that $Ca_2Fe(OH)_6Cl{\cdot}2H_2O$ does not precipitate when $SMR_{Ca/Fe}$ is lower than the isonormal value of 1.5 (see Supporting Information for more details on calculation of isonormal value).

For samples synthesized using high $SMR_{Ca/Fe}$ ratios (i.e., S5 and S10), the XRD patterns in Figure 4 show Bragg peaks that are assigned mostly to crystalline $Ca_2Fe(OH)_6Cl{\cdot}2H_2O$[39] and portlandite[83] (crystalline $Ca(OH)_2$). The corresponding PDF curves in Figure 5 show that these samples are crystalline (i.e., sizable presence of long range ordering), and the local atomic structure reveals peaks at 2.02, 2.38, and ~3.5 Å, which are assigned to the Fe−O bond, the Ca−O bond, and metal−metal (M−M, M = Fe or Ca) correlations, respectively. Interestingly, the M−M peak appears to shift to higher r values in S5 and S10 (from 3.46 Å in S3 to 3.48 Å in S5 and 3.56 Å in S10). This is consistent with the higher amount of unreacted portlandite present in S5 and S10, as portlandite has a lattice parameter of 3.59 Å.[84] The TGA weight loss curves of S5 and S10 in Figure 6 show four distinct decomposition events at around (i) 135, (ii) 285, (iii) 435, and (iv) 630 °C. Characterization of the corresponding evolved gases with FTIR shows that the release of H_2O is responsible for events (i), (ii), and (iii), while CO_2 is released during event (iv) (see Figure 6c,d). By comparing these curves to the decomposition of portlandite, it becomes apparent that peaks (iii) and (iv) correspond to the dehydroxylation of unreacted portlandite and the decomposition of $CaCO_3$, respectively, and that peak

https://doi.org/10.1021/acs.cgd.3c00441
Cryst. Growth Des. 2024, 24, 56−70

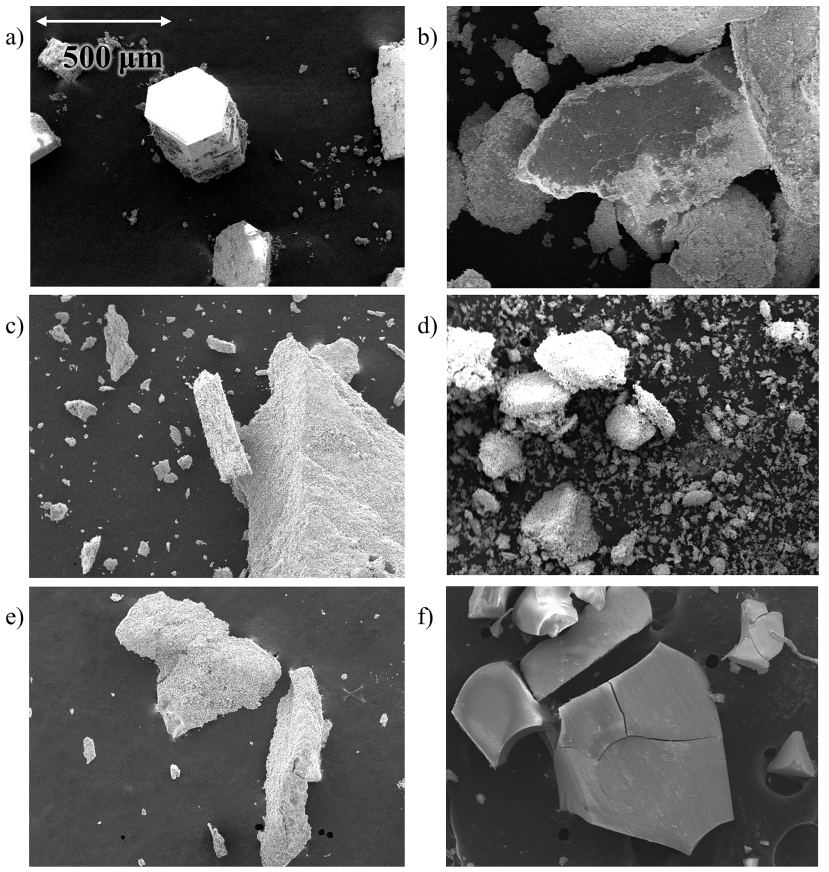

Figure 7. SEM images of (a) recrystallized portlandite, (b) S10, (c) S5, (d) S3, (e) S2, and (f) S1 samples at 100×, showing particle size and shape.

(i) includes contributions from the desorption of surface water.[85] As such, peaks (i) and (ii) for S5 and S10 are assigned to the loss of interlayer water from the LDH (overlapped with surface water) and the dehydroxylation of the LDH, respectively.[86] It is worth mentioning that, although both powders looked identical to the naked eye and yielded supernatant solutions with equal pH, the measured weight loss in the LDH dehydroxylation region for S5 is seen to be higher than S10, with resulting LDH weight compositions being 67 and 52% for S5 and S10, respectively. In other words, for $SMR_{Ca/Fe}$ values where the saturation conditions of $Ca(OH)_{2(s)}$ are met (i.e., the pH of the supernatant solution is buffered to around 12.5), the $FeCl_3$ is the limiting reactant and, thus, a lower $SMR_{Ca/Fe}$ yields a higher sample purity.

The higher purity of the S5 sample compared with S10 also has an impact on particle size and morphology, as seen from SEM imaging. S5 was composed of randomly shaped particles (Figure 7c) with surface mostly covered by stacked thin layers with similar orientation (Figure 8c), while S10 showed a more homogeneous particle size distribution and smooth surface faces (Figure 7b) with localized exfoliated areas (Figure 8b). Although S10 particles do not resemble the hexagonal prisms found in recrystallized portlandite (Figure 7a), it can be seen that the smooth surface morphology of portlandite (Figure 8a) becomes more and more exfoliated as $SMR_{Ca/Fe}$ diminishes, suggesting that the surface of portlandite particles in suspension during synthesis acts as nucleation site for the precipitation of the LDH.

In the case of the S2 sample, the TGA data show a weight loss curve that resembles the decomposition profile of ferrihydrite,[81] however, its XRD pattern shows Bragg peaks of crystalline $Ca_2Fe(OH)_6Cl{\cdot}2H_2O$[39] in addition to the diffuse peaks of 2-line ferrihydrite. PDF analysis further confirms the presence of amorphous ferrihydrite (characteristic Fe−Fe correlation at 3.07 Å) along with the LDH phase, which indicates that a $SMR_{Ca/Fe} = 2$ (supernatant of pH 11, see Table 1) is high enough to enable the precipitation of the LDH, with CaO being the limiting reactant. Given that at pH = 11, the speciation of Fe(III) consists mainly of $Fe(OH)_{3(s)}$ (see Figure 2b), with $[Fe(OH)_4^-] \approx 1.9 \times 10^{-7}$ M (eq 24), it follows that the precipitation of $Ca_2Fe(OH)_6Cl{\cdot}2H_2O$ requires a minimum concentration of $Fe(OH)_4^-$ (or a minimum pH) that has yet to be determined. Interestingly, S2 (Figure 7e) consists of particle shapes and sizes similar to S5 but with a surface morphology composed of thicker and randomly oriented stacked layers (Figure 8e). This could be explained by the impact of pH on the kinetics of the LDH formation.

Finally, S3 is the only sample that shows high phase purity, with an XRD pattern solely containing Bragg peaks of crystalline $Ca_2Fe(OH)_6Cl{\cdot}2H_2O$ (Figure 4) and a PDF lacking the characteristic peak of ferrihydrite (Fe−Fe at 3.07 Å, see Figure 5). Interestingly the location of the LDH M−M peak at 3.46 Å in S3 is in alignment with the second Fe−Fe correlation of 2-line ferrihydrite (3.44 Å[82]) rather than the Ca−Ca in portlandite (at 3.59 Å[84]). The TGA data of S3 show the decomposition events assigned previously to peaks (i) and (ii) as the loss of interlayer/surface water and dehydroxylation of the LDH (with a calculated purity of 91%), and only a small weight loss signal at the position of peak (iii), which is assumed to be the result of a small amount of unreacted

https://doi.org/10.1021/acs.cgd.3c00441
Cryst. Growth Des. 2024, 24, 56−70

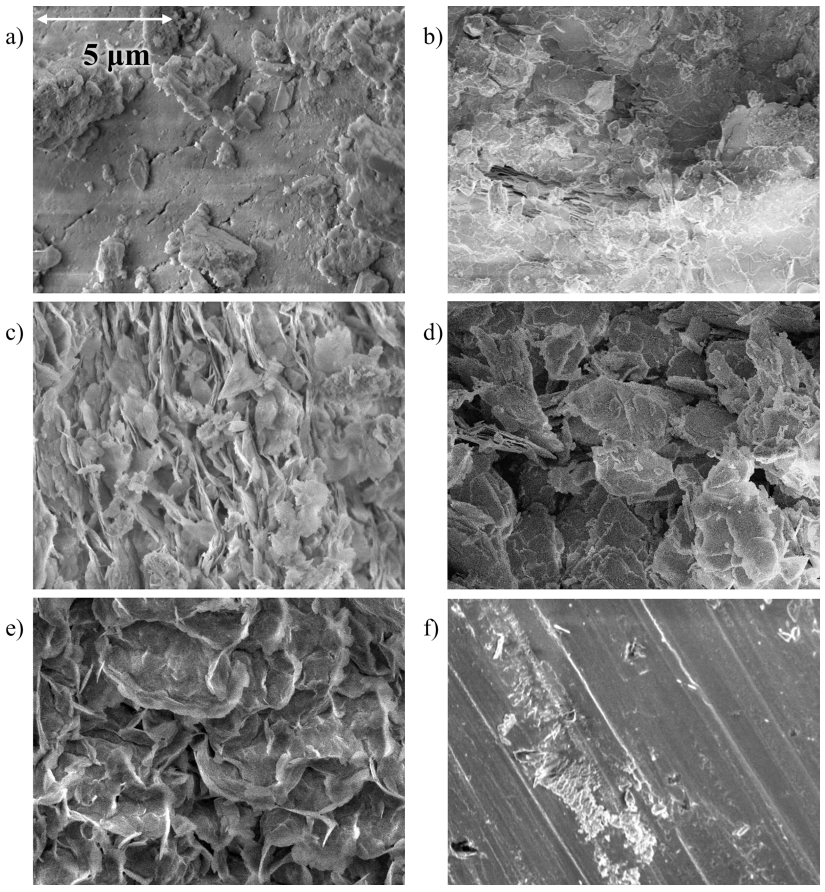

Figure 8. SEM images of (a) recrystallized portlandite, (b) S10, (c) S5, (d) S3, (e) S2, and (f) S1 samples at 5000×, showing surface morphology.

portlandite (about 1.5% of sample composition by weight). Despite our efforts to prevent early carbonation by use of an inert environment during synthesis, peak (iv) is also seen in S3, though it remains unknown whether carbonation occurred during synthesis or during sample loading onto the TGA instrument. In terms of particle size and morphology, S3 is seen to be the finest powder (easiest to grind) among all samples (Figure 7d), composed mainly of plate-like particles with nanosized layer thickness (Figure 8d). This ease of exfoliation (partially observed also for S5 and S2) may originate from the low strength of attraction between the layers in the LDH, which has been previously associated to the large interlayer distance,[7] as opposed to the stronger interactions between layers in portlandite and ferrihydrite. Overall, characterization of samples synthesized using the modified coprecipitation method proposed by Kim et al.[61] with $SMR_{Ca/Fe}$ = 1, 2, 3, 5, and 10 has shown that maximum phase purity is obtained when $SMR_{Ca/Fe}$ = 3. At lower and higher values of $SMR_{Ca/Fe}$, it is found that the phase purity decreases due to the coprecipitation of $Fe(OH)_3$ and $Ca(OH)_2$, respectively.

3.3. Reaction Mechanism. The theoretical speciation analysis presented in Section 3.1, combined with the experimental findings in Section 3.2, provide substantial evidence that the formation mechanism of $Ca_2Fe(OH)_6Cl{\cdot}2H_2O$ synthesized by coprecipitation occurs via a dissolution−reprecipitation reaction sequence as described by eqs 3−6, 10−14, and 29, with the redissolution of $Fe(OH)_{3(s)}$ into $Fe(OH)_{4(aq)}^-$ governing kinetics and an overall $SMR_{Ca/Fe} \approx 3$. Specifically, the elementary steps that lead to the precipitation of the LDH seem to involve the following species: $Fe(OH)_4^-$, Ca^{2+}, OH^-, Cl^-, and H_2O. However, further work is needed to determine the elementary steps comprised in the precipitation reaction.

The constant Bragg peak positions of the $Ca_2Fe(OH)_6Cl{\cdot}2H_2O$ and portlandite phases across samples indicate that the lattice parameters of these crystalline phases do not change with $SMR_{Ca/Fe}$ nor pH. This finding contradicts the post-isomorphic substitution theory for the formation of $Ca_2Fe(OH)_6Cl{\cdot}2H_2O$, which would require the distortion of the portlandite lattice to allow the incorporation of $Fe(OH)_4^-$. Additional evidence supporting this mechanism is the presence of $Ca_2Fe(OH)_6Cl{\cdot}2H_2O$ in S2, where the relatively low pH of the supernatant solution (pH_{S2} = 11) compared to that of S3, S5, and S10 ($pH_{S3,S5,S10}$ = 12.5) lead to the absence of $Ca(OH)_{2(s)}$ but did not impede the formation of the LDH. Contrarily, a dissolution−precipitation can explain the increased relative intensity of the $Ca_2Fe(OH)_6Cl{\cdot}2H_2O$ Bragg peaks with respect to the portlandite peaks as the $SMR_{Ca/Fe}$ decreases until the stoichiometric value of ≈3 is reached. Furthermore, the high phase purity of S3, observed using XRD, PDF analysis, and TGA−FTIR, supports the accuracy of the stoichiometric $SMR_{Ca/Fe} \approx 3$ calculated in Section 3.1.4.

As for the species involved, the absence of LDH in S1 (which yielded a supernatant solution with pH = 2.5) confirms that neither $FeOH^{2+}{}_{(aq)}$, $Fe(OH)_2^+{}_{(aq)}$, or $Fe(OH)_{3(s)}$ participate in the precipitation step of $Ca_2Fe(OH)_6Cl{\cdot}2H_2O$. The

https://doi.org/10.1021/acs.cgd.3c00441
Cryst. Growth Des. 2024, 24, 56−70

surface and particle morphologies of S10 and S5 observed through SEM (Figures 7 and 8) suggest that nucleation occurs to some extent on the surface of portlandite particles, likely due to the higher concentration of Ca(II) species in solution in the vicinity of these particles. However, further investigation is required to determine which Ca(II) species take part in the precipitation step of $Ca_2Fe(OH)_6Cl{\cdot}2H_2O$ and where are the more favorable sites for nucleation to occur.

3.4. Synthesis and Characterization of Phase-Pure $Ca_2Fe(OH)_6Cl{\cdot}2H_2O$. Although the modified precipitation method presented in Section 2.1.1 was deemed successful in synthesizing crystalline $Ca_2Fe(OH)_6Cl{\cdot}2H_2O$ of considerable purity without the use of NaOH, the dropwise mixing, which requires an inert environment to avoid early carbonation of the alkaline Ca(II)-bearing suspension, poses a challenge for its reproducibility at scale. With the goal of simplifying the synthesis method of Ca-LDHs without compromising sample purity, here, we attempted to synthesize $Ca_2Fe(OH)_6Cl{\cdot}2H_2O$ (referred as SFeCl hereafter) using a one-pot method without the need for an inert environment or dropwise mixing. Phase purity has been assessed by means of TGA and synchrotron-based HR-XRD analyzed using Bruker DIFFRAC.EVA software.

The HR-XRD pattern of the synthesized SFeCl sample (presented in Figure 9) shows only the expected Bragg reflections of the crystal structure for $Ca_2Fe(OH)_6Cl{\cdot}2H_2O$.[39] The absence of Bragg peaks corresponding to $CaCO_3$ polymorphs indicates that replacing the alkaline suspension with the solid source of Ca(II) did not increase early carbonation, even without the use of an inert environment. Moreover, the absence of other Bragg peaks and diffuse peaks, previously correlated with the presence of portlandite and amorphous $Fe(OH)_3$, provides further evidence that the stoichiometric $SMR_{Ca/Fe} \approx 3$ estimated in Section 3.1.4 leads to the formation of phase-pure $Ca_2Fe(OH)_6Cl{\cdot}2H_2O$.

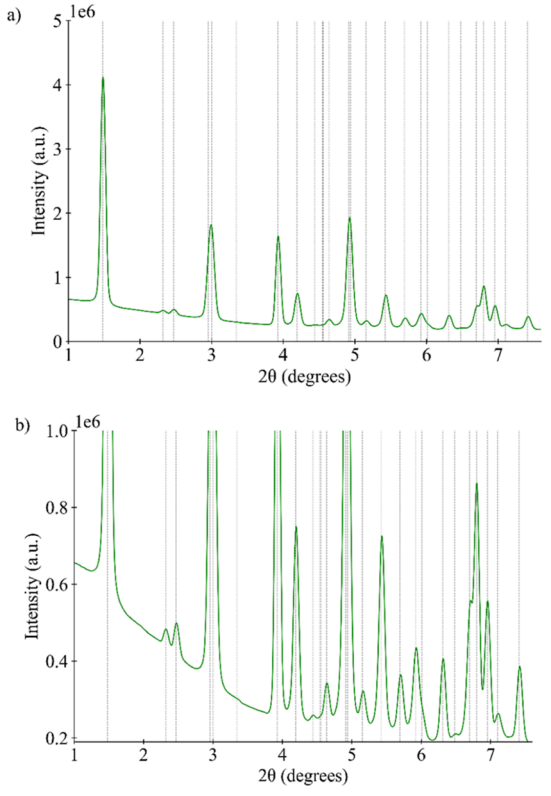

Figure 9. Synchrotron-based HR-XRD (λ = 0.2004 Å) pattern of SFeCl. Bragg peaks were assigned using Bruker DIFFRAC.EVA software ($R\bar{3}$ symmetry with a = 5.848 and c = 23.382 Å). The positions of the LDH Bragg peaks are shown in gray. (b) Is a zoom of (a) to highlight the smaller Bragg peaks present in the XRD pattern of the LDH phase.

4. CONCLUSIONS

Ca-LDHs are of great industrial interest due to their enhanced catalytic activity and chemical versatility. However, the available synthesis methods are hard to scale up for production, have significant environmental impact, and fail at producing phase-pure materials that are associated with enhanced adsorption capacity. In this work, we studied the speciation analysis of the precursors in solution during the synthesis of $Ca_2Fe(OH)_6Cl{\cdot}2H_2O$ from $FeCl_{3(aq)}$ and $Ca(OH)_{2(aq)}$. Our calculations indicate that a Ca/Fe(III) solution molar ratio $(SMR_{Ca/Fe}) = 3 + V\frac{(0.005\ M)}{n_{FeCl_3}}$ and a solution volume $(V) > \frac{n_{FeCl_3}}{0.04\ M}$ are necessary to achieve full conversion of the Fe(III) species in solution (n_{FeCl_3}) without yielding an excess of $Ca(OH)_{2(s)}$. The theoretical $SMR_{Ca/Fe}$ value is based on the chemical equilibria of species in solution and the normality of the precursors to ensure sufficient OH^- equivalents to drive the precipitation of the Ca-LDH.

We subsequently investigated the effect of $SMR_{Ca/Fe}$ on LDH sample purity and crystallinity by means of TGA coupled with gas Fourier transform infrared spectroscopy (TGA–FTIR), X-ray diffraction (XRD), pair distribution function (PDF) analysis, and scanning electron microscopy (SEM). Characterization of powder samples and observations made during synthesis are in agreement with our theoretically calculated stoichiometric $SMR_{Ca/Fe} \approx 3$ and strongly support an LDH formation mechanism consisting of precursor dissolution followed by LDH precipitation from solution (i.e., dissolution–reprecipitation). Finally, we introduced a new method for the synthesis of phase-pure crystalline Ca-LDHs that avoids the use of NaOH and can be easily modified to obtain samples of various chemistries. The new method consists of a one-pot synthesis based on the in situ hydrolysis of $Ca(OH)_2$ without the need for an inert environment. Synchrotron-based high-resolution XRD showed that phase-pure $Ca_2Fe(OH)_6Cl{\cdot}2H_2O$ was obtained using this new method.

■ ASSOCIATED CONTENT

Supporting Information

The Supporting Information is available free of charge at https://pubs.acs.org/doi/10.1021/acs.cgd.3c00441.

Determination of isonormal $SMR_{Ca/Fe}$ and model-fitting of TGA data (PDF)

■ AUTHOR INFORMATION

Corresponding Author

Claire E. White − *Department of Civil and Environmental Engineering, Princeton University, Princeton, New Jersey 08544, United States; Andlinger Center for Energy and the Environment, Princeton University, Princeton, New Jersey 08544, United States;* orcid.org/0000-0002-4800-7960;

https://doi.org/10.1021/acs.cgd.3c00441
Cryst. Growth Des. 2024, 24, 56−70

Phone: +1 609 258 6263; Email: whitece@princeton.edu; Fax: +1 609 258 2799

Author

Maria C. Curria − *Department of Civil and Environmental Engineering, Princeton University, Princeton, New Jersey 08544, United States; Andlinger Center for Energy and the Environment, Princeton University, Princeton, New Jersey 08544, United States;* orcid.org/0000-0002-3080-8508

Complete contact information is available at: https://pubs.acs.org/10.1021/acs.cgd.3c00441

Notes

The authors declare no competing financial interest.

■ ACKNOWLEDGMENTS

This work was financially supported by the Princeton E-ffiliates Partnership award, Andlinger Center for Energy and the Environment (Princeton University), and National Science Foundation grant no. 1553607. The authors acknowledge the use of Princeton's Imaging and Analysis Center, which is partially supported through the Princeton Center for Complex Materials (PCCM), a National Science Foundation (NSF)-MRSEC program (DMR-2011750). This research used resources of the Advanced Photon Source, a U.S. Department of Energy (DOE) Office of Science User Facility operated for the DOE Office of Science by Argonne National Laboratory under Contract no. DE-AC02-06CH11357. The authors acknowledge the European Synchrotron Radiation Facility (ESRF) for provision of synchrotron radiation facilities and they thank Catherine Dejoie for assistance and support in using beamline ID22.

■ ABBREVIATION

α_i	extent of conversion (decomposition) of the compound i
k_{o_i}	preexponential factor of the Arrhenius rate constant for the decomposition i (s^{-1})
E_i^o	activation energy of the Arrhenius rate constant for the decomposition i (J mol^{-1})
R	gas constant [J $(mol\ K)^{-1}$]
T	temperature (K)
β	heating rate (K s^{-1})
K_i	equilibrium constant of compound i
K_{SPi}	solubility product constant of compound i
K_w	equilibrium constant of water
SMR	solution molar ratio
M	molarity (mol L^{-1})
M_{eq}	molarity equivalent (for a suspension) (mol L^{-1})

■ REFERENCES

(1) Komarneni, S.; Kozai, N.; Roy, R. Novel function for anionic clays: selective transition metal cation uptake by diadochy. *J. Mater. Chem.* **1998**, *8*, 1329−1331.

(2) Lakraimi, M.; Legrouri, A.; Barroug, A.; De Roy, A.; Pierre Besse, J. Preparation of a new stable hybrid material by chloride−2,4-dichlorophenoxyacetate ion exchange into the zinc−aluminium−chloride layered double hydroxide. *J. Mater. Chem.* **2000**, *10*, 1007−1011.

(3) Ait Bentaleb, K.; El Khattabi, E.; Lakraimi, M.; Benaziz, L.; Sabbar, E.; Berraho, M.; et al. Removal of Cr(VI) from wastewater by anionic clays. *J. Mater. Environ. Sci.* **2016**, *7*, 2886−2896.

(4) Wang, Y.; Yang, W.; Chen, C.; Evans, D. G. Fabrication and electrochemical characterization of cobalt-based layered double hydroxide nanosheet thin-film electrodes. *J. Power Sources* **2008**, *184*, 682−690.

(5) Xu, Z. P.; Zhang, J.; Adebajo, M. O.; Zhang, H.; Zhou, C. Catalytic applications of layered double hydroxides and derivatives. *Appl. Clay Sci.* **2011**, *53*, 139−150.

(6) Liang, X.; Zang, Y.; Xu, Y.; Tan, X.; Hou, W.; Wang, L.; Sun, Y. Sorption of metal cations on layered double hydroxides. *Colloids Surf., A* **2013**, *433*, 122−131.

(7) Long, X.; Wang, Z.; Xiao, S.; An, Y.; Yang, S. Transition metal based layered double hydroxides tailored for energy conversion and storage. *Mater. Today* **2016**, *19*, 213−226.

(8) Tao, P.; Yao, S.; Liu, F.; Wang, B.; Huang, F.; Wang, M. Recent advances in exfoliation techniques of layered and non-layered materials for energy conversion and storage. *J. Mater. Chem. A* **2019**, *7*, 23512−23536.

(9) Chen, H.; Hu, L.; Chen, M.; Yan, Y.; Wu, L. Nickel-cobalt layered double hydroxide nanosheets for high-performance supercapacitor electrode materials. *Adv. Funct. Mater.* **2014**, *24*, 934−942.

(10) Abushrenta, N.; Wu, X.; Wang, J.; Liu, J.; Sun, X. Hierarchical Co-based Porous Layered Double Hydroxide Arrays Derived via Alkali Etching for High-performance Supercapacitors. *Sci. Rep.* **2015**, *5*, 13082.

(11) Dionigi, F.; Zeng, Z.; Sinev, I.; Merzdorf, T.; Deshpande, S.; Lopez, M. B.; Kunze, S.; Zegkinoglou, I.; Sarodnik, H.; Fan, D.; et al. In-situ structure and catalytic mechanism of NiFe and CoFe layered double hydroxides during oxygen evolution. *Nat. Commun.* **2020**, *11*, 2522.

(12) Ahmed, N.; Shibata, Y.; Taniguchi, T.; Izumi, Y. Photocatalytic conversion of carbon dioxide into methanol using zinc-copper-M(III) (M = aluminum, gallium) layered double hydroxides. *J. Catal.* **2011**, *279*, 123−135.

(13) Zhao, Y.; Zhao, Y.; Waterhouse, G. I. N.; Zheng, L.; Cao, X.; Teng, F.; Wu, L. Z.; Tung, C. H.; O'Hare, D.; Zhang, T. Layered-double-hydroxide nanosheets as efficient visible-light-driven photocatalysts for dinitrogen fixation. *Adv. Mater.* **2017**, *29*, 1703828.

(14) López-Salinas, E.; Serrano, M. E. L.; Jácome, M. A. C.; Secora, I. S. Characterization of synthetic hydrocalumite-type $[Ca_2Al(OH)_6]$-$NO_3{\cdot}mH_2O$: Effect of the calcination temperature. *J. Porous Mater.* **1996**, *2*, 291−297.

(15) Md Ghazali, I. W.; Bohari, F. L.; Dzulkifli, N. N.; Abdullah, A.; Fatimah, I.; Sheikh Mohd Ghazali, S. A. I. Synthesis and applications of calcium-aluminum layered double hydroxides - an overview). *Polymers* **2021**, *66*, 518−526.

(16) Park, J. Y.; Yoo, S. B.; Cho, H. B.; Lee, H. S.; Choa, Y. H. CaFe-based layered double oxides with superior iron alloy corrosion inhibition behaviors in aggressive seawater environment. *Front. Chem.* **2022**, *10*, 1−12.

(17) Kim, G.; Park, S. Chloride removal of calcium aluminate-layered double hydroxide phases: A review. *Int. J. Environ. Res. Public Health* **2021**, *18*, 2797.

(18) Lu, H.; Liu, S.; Zhang, H.; Qiu, Y.; Zhao, J.; Zhu, Z. Decontamination of arsenic in actual water samples by calcium containing layered double hydroxides from a convenient synthesis method. *Water* **2018**, *10*, 1150.

(19) Narayanappa, A. N.; Kamath, P. V. Interaction of pristine hydrocalumite-like layered double hydroxides with carbon dioxide. *ACS Omega* **2019**, *4*, 3198−3204.

(20) Rossi, T. M.; Campos, J. C.; Souza, M. M. V. M. An evaluation of calcined hydrocalumite as carbon dioxide adsorbent using thermogravimetric analysis. *Appl. Clay Sci.* **2019**, *182*, 105252.

(21) Manohara, G. V.; Maroto-Valer, M. M.; Garcia, S. The effect of the layer-interlayer chemistry of LDHs on developing high temperature carbon capture materials. *Dalton Trans.* **2020**, *49*, 923−931.

(22) Yang, Z. z.; Wei, J. j.; Zeng, G. m.; Zhang, H. q.; Tan, X. f.; Ma, C.; Li, X. c.; Li, Z. h.; Zhang, C. A review on strategies to LDH-based materials to improve adsorption capacity and photoreduction efficiency for CO_2. *Coord. Chem. Rev.* **2019**, *386*, 154−182.

(23) Matschei, T.; Lothenbach, B.; Glasser, F. P. The AFm phase in Portland cement. *Cem. Concr. Res.* **2007**, *37*, 118−130.

(24) Reichle, W. T. Synthesis of anionic clay minerals (mixed metal hydroxides, hydrotalcite). *Solid State Ionics* **1986**, *22*, 135−141.
(25) Miyata, S. The syntheses of hydrotalcite-like compounds and their structures and physico-chemical properties I: the systems Mg^{2+}-Al^{3+}-NO^{3-}, Mg^{2+}-Al^{3+}-Cl^{-}, Mg^{2+}-Al^{3+}-ClO_4^{-}, Ni^{2+}-Al^{3+}-Cl^{-} and Zn^{2+}-Al^{3+}-Cl^{-}. *Clays Clay Miner.* **1975**, *23*, 369−375.
(26) Miyata, S.; Okada, A. Synthesis of hydrotalcite-like compounds and their physico-chemical properties—the systems Mg^{2+}-Al^{3+}-SO_4^{2-} and Mg^{2+}-Al^{3+}-CrO_4^{2-}. *Clays Clay Miner.* **1977**, *25*, 14−18.
(27) Miyata, S.; Hirose, T. Adsorption of N_2, O_2, CO_2 and H_2 on hydrotalcite-like system: Mg^{2+}-Al^{3+}-$(Fe(CN)_6)_4$. *Clays Clay Miner.* **1978**, *26*, 441−447.
(28) Jaiswal, A.; Gautam, R. K.; Chattopadhyaya, M. C. Layered Double Hydroxides and the Environment: An Overview. *Advanced Materials for Agriculture, Food, and Environmental Safety*; John Wiley & Sons, Ltd, 2014; pp 1−26.
(29) Mishra, G.; Dash, B.; Pandey, S. Layered double hydroxides: A brief review from fundamentals to application as evolving biomaterials. *Appl. Clay Sci.* **2018**, *153*, 172−186.
(30) Othman, M. R.; Helwani, Z.; Martunus; Fernando, W. J. N. Synthetic hydrotalcites from different routes and their application as catalysts and gas adsorbents: a review. *Appl. Organomet. Chem.* **2009**, *23*, 335−346.
(31) Muráth, S.; Somosi, Z.; Kukovecz, Á.; Kónya, Z.; Sipos, P.; Pálinkó, I. Novel route to synthesize CaAl- and MgAl-layered double hydroxides with highly regular morphology. *J. Sol-Gel Sci. Technol.* **2019**, *89*, 844−851.
(32) Cota, I.; Ramírez, E.; Medina, F.; Sueiras, J. E.; Layrac, G.; Tichit, D. New synthesis route of hydrocalumite-type materials and their application as basic catalysts for aldol condensation. *Appl. Clay Sci.* **2010**, *50*, 498−502.
(33) Wang, J.; Stevens, L. A.; Drage, T. C.; Wood, J. Preparation and CO2 adsorption of amine modified Mg−Al LDH via exfoliation route. *Chem. Eng. Sci.* **2012**, *68*, 424−431.
(34) Fahami, A.; Beall, G. W.; Enayatpour, S.; Tavangarian, F.; Fahami, M. Rapid preparation of nano hexagonal-shaped hydrocalumite via one-pot mechanochemistry method. *Appl. Clay Sci.* **2017**, *136*, 90−95.
(35) Zadaviciute, S.; Baltakys, K.; Bankauskaite, A. The effect of microwave and hydrothermal treatments on the properties of hydrotalcite. *J. Therm. Anal. Calorim.* **2017**, *127*, 189−196.
(36) Feitknecht, W.; Gerber, M. Zur Kenntnis der Doppelhydroxyde und basischen Doppelsalze III. Über Magnesium-Aluminiumdoppelhydroxyd. *Helv. Chim. Acta* **1942**, *25*, 131−137.
(37) Brown, G.; Gastuche, M. C. Mixed magnesium-aluminium hydroxides. II. Structure and structural chemistry of synthetic hydroxycarbonates and related minerals and compounds. *Clay Miner.* **1967**, *7*, 193−201.
(38) Xu, Z. P.; Lu, G. Q. M. Hydrothermal Synthesis of Layered Double Hydroxides (LDHs) from Mixed MgO and Al_2O_3: LDH Formation Mechanism. *Chem. Mater.* **2005**, *17*, 1055−1062.
(39) Rousselot, I.; Taviot-Guého, C.; Leroux, F.; Léone, P.; Palvadeau, P.; Besse, J.-P. Insights on the structural chemistry of hydrocalumite and hydrotalcite-like materials: Investigation of the series $Ca_2M^{3+}(OH)_6Cl{\cdot}2H_2O$ (M^{3+}: Al^{3+}, Ga^{3+}, Fe^{3+}, and Sc^{3+}) by X-ray powder diffraction. *J. Solid State Chem.* **2002**, *167*, 137−144.
(40) Szabados, M.; Adél Ádám, A.; Traj, P.; Muráth, S.; Baán, K.; Bélteky, P.; Kónya, Z.; Kukovecz, Á.; Sipos, P.; Pálinkó, I. Mechanochemical and wet chemical syntheses of CaIn-layered double hydroxide and its performance in a transesterification reaction compared to those of other Ca2M(III) hydrocalumites (M: Al, Sc, V, Cr, Fe, Ga) and Mg(II)-Ni(II)-Co(II)- or Zn(II)-based hydrotalcites. *J. Catal.* **2020**, *391*, 282−297.
(41) Miyata, S.; Kumura, T. Synthesis of new hydrotalcite-like compounds and their physico-chemical properties. *Chem. Lett.* **1973**, *2*, 843−848.
(42) Manohara, G. V.; Li, L.; Whiting, A.; Greenwell, H. C. Ultra-high aspect ratio hybrid materials: the role of organic guest and synthesis method. *Dalton Trans.* **2018**, *47*, 2933−2938.
(43) Sipiczki, M.; Kuzmann, E.; Homonnay, Z.; Megyeri, J.; Pálinkó, I.; Sipos, P. The structure and stability of CaFe layered double hydroxides with various Ca:Fe ratios studied by Mössbauer spectroscopy, X-ray diffractometry and microscopic analysis. *J. Mol. Struct.* **2013**, *1044*, 116−120.
(44) Tóth, V.; Sipiczki, M.; Pallagi, A.; Kukovecz, Á.; Kónya, Z.; Sipos, P.; Pálinkó, I. Synthesis and properties of CaAl-layered double hydroxides of hydrocalumite-type. *Chem. Pap.* **2014**, *68*, 633.
(45) Pang, X.; Liu, Y.; Chen, L.; Zhong, Y.; Li, Z.; Liu, M.; Li, S. Preparation and formation mechanism of pure phase Ca2Al-layered double hydroxides nanosheets synthesized by a T-type microchannel reactor: Application as hardening accelerator for mortar. *Appl. Clay Sci.* **2018**, *166*, 174−180.
(46) Theiss, F. L.; Ayoko, G. A.; Frost, R. L. Synthesis of layered double hydroxides containing Mg^{2+}, Zn^{2+}, Ca^{2+} and Al^{3+} layer cations by co-precipitation methods—A review. *Appl. Surf. Sci.* **2016**, *383*, 200−213.
(47) Gevers, B. R.; Labuschagné, F. J. W. J. Green Synthesis of Hydrocalumite (CaAl-OH-LDH) from $Ca(OH)_2$ and $Al(OH)_3$ and the Parameters That Influence Its Formation and Speciation. *Crystals* **2020**, *10*, 672.
(48) Labuschagné, F. J. W. J.; Wiid, A.; Venter, H. P.; Gevers, B. R.; Leuteritz, A. Green synthesis of hydrotalcite from untreated magnesium oxide and aluminum hydroxide. *Green Chem. Lett. Rev.* **2018**, *11*, 18−28.
(49) Benito, P.; Guinea, I.; Herrero, M.; Labajos, F. M.; Rives, V. Incidence of microwave hydrothermal treatments on the crystallinity properties of hydrotalcite-like compounds. *Z. fur Anorg. Allg. Chem.* **2007**, *633*, 1815−1819.
(50) Cavani, F.; Trifirò, F.; Vaccari, A. Hydrotalcite-type anionic clays: Preparation, properties and applications. *Catal. Today* **1991**, *11*, 173−301.
(51) Trujillano, R.; González-García, I.; Morato, A.; Rives, V. Controlling the synthesis conditions for tuning the properties of hydrotalcite-like materials at the nano scale. *ChemEngineering* **2018**, *2*, 31.
(52) Benito, P.; Herrero, M.; Barriga, C.; Labajos, F. M.; Rives, V. Microwave-assisted homogeneous precipitation of hydrotalcites by urea hydrolysis. *Inorg. Chem.* **2008**, *47*, 5453−5463.
(53) Costantino, U.; Marmottini, F.; Nocchetti, M.; Vivani, R. New synthetic routes to hydrotalcite-like compounds − characterisation and properties of the obtained materials. *Eur. J. Inorg. Chem.* **1998**, *1998*, 1439−1446.
(54) Staal, L. B.; Charan Pushparaj, S. S.; Forano, C.; Prevot, V.; Ravnsbæk, D. B.; Bjerring, M.; Nielsen, U. G. Competitive reactions during synthesis of zinc aluminum layered double hydroxides by thermal hydrolysis of urea. *J. Mater. Chem. A* **2017**, *5*, 21795−21806.
(55) Inayat, A.; Klumpp, M.; Schwieger, W. The urea method for the direct synthesis of ZnAl layered double hydroxides with nitrate as the interlayer anion. *Appl. Clay Sci.* **2011**, *51*, 452−459.
(56) Hibino, T.; Ohya, H. Synthesis of crystalline layered double hydroxides: Precipitation by using urea hydrolysis and subsequent hydrothermal reactions in aqueous solutions. *Appl. Clay Sci.* **2009**, *45*, 123−132.
(57) Ferencz, Z.; Kukovecz, Á.; Kónya, Z.; Sipos, P.; Pálinkó, I. Optimisation of the synthesis parameters of mechanochemically prepared CaAl-layered double hydroxide. *Appl. Clay Sci.* **2015**, *112−113*, 94−99.
(58) Aramendía, M. Comparative study of Mg/M(III) (M=Al, Ga, In) layered double hydroxides obtained by coprecipitation and the sol−gel method. *J. Solid State Chem.* **2002**, *168*, 156−161.
(59) Prinetto, F.; Ghiotti, G.; Graffin, P.; Tichit, D. Synthesis and characterization of sol−gel Mg/Al and Ni/Al layered double hydroxides and comparison with co-precipitated samples. *Microporous Mesoporous Mater.* **2000**, *39*, 229−247.
(60) Jitianu, A.; Britchi, A.; Deleanu, C.; Badescu, V.; Zaharescu, M. Comparative study of the sol−gel processes starting with different substituted Si-alkoxides. *J. Non-Cryst. Solids* **2003**, *319*, 263−279.

https://doi.org/10.1021/acs.cgd.3c00441
Cryst. Growth Des. 2024, 24, 56−70

(61) Kim, J. H.; Park, M.; Imran, A.; Choi, M.-C.; Kim, K. S.; Komarneni, S. Post-isomorphic substitution of trivalent metal cations for Ca^{2+} in portlandite crystals. *RSC Adv.* **2014**, *4*, 29305−29309.
(62) Chupas, P. J.; Chapman, K. W.; Lee, P. L. Applications of an amorphous silicon-based area detector for high-resolution, high-sensitivity and fast time-resolved pair distribution function measurements. *J. Appl. Crystallogr.* **2007**, *40*, 463−470.
(63) Toby, B. H.; Von Dreele, R. B. GSAS-II: the genesis of a modern open-source all purpose crystallography software package. *J. Appl. Crystallogr.* **2013**, *46*, 544−549.
(64) Qiu, X.; Thompson, J. W.; Billinge, S. J. L. PDFgetX2 : a GUI-driven program to obtain the pair distribution function from X-ray powder diffraction data. *J. Appl. Crystallogr.* **2004**, *37*, 678.
(65) Hodeau, J.-L.; Bordet, P.; Anne, M.; Prat, A.; Fitch, A. N.; Dooryhee, E.; Vaughan, G.; Freund, A. K. Nine-crystal multianalyzer stage for high-resolution powder diffraction between 6 keV and 40 keV. *Cryst Multilayer Opt* **1998**, *3448*, 353.
(66) Vyazovkin, S. Modification of the integral isoconversional method to account for variation in the activation energy. *J. Comput. Chem.* **2000**, *22*, 178−183.
(67) Kutus, B.; Gácsi, A.; Pallagi, A.; Pálinkó, I.; Peintler, G.; Sipos, P. A comprehensive study on the dominant formation of the dissolved $Ca(OH)_{2(aq)}$ in strongly alkaline solutions saturated by Ca(II). *RSC Adv.* **2016**, *6*, 45231−45240.
(68) Lito, M. J. G. H. M.; Camões, M. F. G. F. C.; Covington, A. K. Equilibrium in saturated $Ca(OH)_2$ solutions: Parameters and dissociation constants. *J. Solution Chem.* **1998**, *27*, 925−933.
(69) Bell, R. P.; George, J. H. B. The incomplete dissociation of some thallous and calcium salts at different temperatures. *Trans. Faraday Soc.* **1953**, *49*, 619.
(70) Davies, C. W.; Hoyle, B. E. 51. The dissociation constant of calcium hydroxide. *J. Chem. Soc.* **1951**, 231−238.
(71) Davies, C. W. 56. The extent of dissociation of salts in water. Part VI. Some calcium salts of organic acids. *J. Chem. Soc.* **1938**, *277*, 277.
(72) Bates, R. G.; Bower, V. E.; Canham, R. G.; Prue, J. E. The dissociation constant of $CaOH^+$ from 0 ° to 40 °C. *Trans. Faraday Soc.* **1959**, *55*, 2062−2068.
(73) Davies, C. W. 280. The electrolytic dissociation of metal hydroxides. *J. Chem. Soc.* **1951**, 1256.
(74) Gimblett, F. G. R.; Monk, C. B. E.m.f. studies of electrolytic dissociation. Part 7.—Some alkali and alkaline earth metal hydroxides in water. *Trans. Faraday Soc.* **1954**, *50*, 965−972.
(75) Kilde, G. Ein Verfahren zur Bestimmung der Calciumionenkonzentration und ihre Anwendung zur Bestimmung der Dissoziation des Calciumhydroxyds. *Z. fur Anorg. Allg. Chem.* **1934**, *218*, 113−128.
(76) Solubility product constants of inorganic salts. In *CRC Handbook of Chemistry and Physics Book*, 103rd ed.; Rumble, J. R., Ed; CRC Press, 2022.
(77) Meites, L. *Handbook of Analytical Chemistry*; McGraw-Hill: New York, 1963.
(78) Oriekhova, O.; Stoll, S. Investigation of FeCl3 induced coagulation processes using electrophoretic measurement, nanoparticle tracking analysis and dynamic light scattering: Importance of pH and colloid surface charge. *Colloids Surf., A* **2014**, *461*, 212−219.
(79) Stefánsson, A. Iron(III) Hydrolysis and Solubility at 25 °C. *Environ. Sci. Technol.* **2007**, *41*, 6117−6123.
(80) Hem, J. D., *Chemistry of iron in natural water*. U.S. Goverment Publishing Office. Water Supply Pap 1459-I, 1962; p 268.
(81) Cornell, R. M.; Schwertmann, U. *The Iron Oxides: Structure, Properties, Reactions, Occurrences and Uses*, 2nd ed., Completely Revised and Extended Edition; Wiley, 2006.
(82) Michel, F. M.; Ehm, L.; Liu, G.; Han, W. Q.; Antao, S. M.; Chupas, P. J.; Lee, P. L.; Knorr, K.; Eulert, H.; Kim, J.; et al. Similarities in 2- and 6-line ferrihydrite based on pair distribution function analysis of x-ray total scattering. *Chem. Mater.* **2007**, *19*, 1489−1496.
(83) Ruiz-Agudo, E.; Kudłacz, K.; Putnis, C. V.; Putnis, A.; Rodriguez-Navarro, C. Dissolution and carbonation of portlandite $[Ca(OH)_2]$ single crystals. *Environ. Sci. Technol.* **2013**, *47*, 11342−11349.
(84) Galmarini, S.; Aimable, A.; Ruffray, N.; Bowen, P. Changes in portlandite morphology with solvent composition: Atomistic simulations and experiment. *Cem. Concr. Res.* **2011**, *41*, 1330−1338.
(85) Morales-Flórez, V.; Santos, A.; Romero-Hermida, I.; Esquivias, L. Hydration and carbonation reactions of calcium oxide by weathering: Kinetics and changes in the nanostructure. *Chem. Eng. J.* **2015**, *265*, 194−200.
(86) Ram Reddy, M. K.; Xu, Z. P.; Lu, G. Q. M.; Diniz da Costa, J. C. Layered Double Hydroxides for CO_2 Capture: Structure Evolution and Regeneration. *Ind. Eng. Chem. Res.* **2006**, *45*, 7504−7509.

https://doi.org/10.1021/acs.cgd.3c00441
Cryst. Growth Des. 2024, 24, 56−70